國立交通大學

電子物理研究所

博士論文

披覆銻砷化鎵之砷化銦量子點的能帶結構工程及元件應用

Band Structure Engineering and Device Applications of

GaAsSb-Capped InAs Quantum Dots

研究生:廖昱安

指導教授:綦振瀛 博士

張文豪 博士

中華民國 一百零二 年 九 月

披覆銻砷化鎵之砷化銦量子點的能帶結構工程及元件應用

Band Structure Engineering and Device Applications of GaAsSb-Capped InAs Quantum Dots

研究生：廖昱安　　Student：Yu-An Liao

指導教授：綦振瀛 博士　　Advisors：Dr. Jen-Inn Chyi

張文豪 博士　　Dr. Wen-Hao Chang

國立交通大學

電子物理研究所

博士論文

A Thesis

Submitted to Institute of Electrophysics

College of Science

National Chiao Tung University

in partial Fulfillment of the Requirements

for the Degree of

Doctor of Philosophy

in

Electrophysics

September 2013

Hsinchu, Taiwan, Republic of China

中華民國 一百零二 年 九 月

披覆銻砷化鎵之砷化銦量子點的能帶結構工程及元件應用

研究生：廖昱安　　指導教授：綦振瀛 博士
張文豪 博士

國立交通大學 電子物理研究所博士班

摘要

本論文旨在探討披覆銻砷化鎵之砷化銦量子點的能帶結構調變工程及其元件應用，主要內容包含兩個主題。在論文的第一個部分，我們利用四種方法去調變披覆銻砷化鎵之砷化銦量子點的能帶結構。首先，我們改變銻砷化鎵披覆層中銻的組成，並由時間解析光譜技術研究載子的動態行為，無論由變功率光激螢光光譜峰值的位移或由較長的時間衰減常數，都證實了在異質接面所形成的第二型能帶結構；不同的載子復合路徑也藉由變溫量測得以區分。第二種方法為熱退火處理。除了明顯的螢光峰值藍位移及光譜線寬縮減外，熱退火所引起的合金混合也造成輻射復合速率的增加及消除在銻砷化鎵披覆層的載子侷限態。同時，在變功率及時間解析螢光的量測中，我們也觀察到由第二型變成第一型的能帶結構變化。第三種方法為披覆層厚度的調變。我們發現發射光的能量和載子復合生命期都與披覆層厚度有密切的關係。理論計算也指出量子侷限和電洞波函數分佈對披覆層厚度的變化相當敏感。同時，銻原子造成的量子點尺寸變化在其光學特性上也扮演相當重要的角色。最後我們採用了銻砷化鋁鎵四元化合物披覆層。由變功率及時間解析螢光量測的結果，披覆銻砷化鎵之砷化銦量子點的第二型能帶結構能藉由加入鋁元素而轉變為第一型能帶結構，而這個能帶結構的轉變也同時從理論計算得到證實。

披覆銻砷化鎵之砷化銦量子點的元件應用為本論文第二部分的重點。首先，我們探討披覆砷化鎵層之砷化銦紅外線量子點光檢測器的光譜響應。相較於傳統的砷化銦紅外線量子點光檢測器，其呈現較窄的光譜線寬和較長的檢測波長，這些變化可歸因於銻砷化鎵披覆層造成之尺寸較大且較均勻的量子點。同時，我們也藉由光激螢光激發光譜得知其光譜響應的躍遷機制來源。另外一個應用為記憶體元件。為了簡化製程手續，我們採用了寬通道平面式柵極電晶體的技術來研究披覆銻砷化鎵之砷化銦量子點的記憶體效應。因此在探討記憶體元件前，我們先介紹俱砷化鎵片電阻之平面式柵極電晶體。在有效控制片電阻的摻雜濃度情況下，理想的電流調變特性和高集極電流之間可取得平衡。其調變開關特性的機制，是藉由操控表面自由電子分佈來空乏元件通道。此外，光電流的量測結果也顯示出該技術有應用於光檢測器的潛力。在對寬通道平面式柵極電晶體了解後，我們展示室溫下使用寬通道平面式柵極電晶體之砷化銦量子點充放電的能力。相較於第一型量子點，俱銻砷化鎵披覆層之第二型量子點呈現出較長的充放電時間。由披覆銻砷化鎵之砷化銦量子點提供之較慢的電荷弛豫和簡化的平面式柵極電晶體技術，揭示該元件俱有實際應用的潛力。

Band Structure Engineering and Device Applications of GaAsSb-Capped InAs Quantum Dots

Student: Yu-An Liao Advisors: Dr. Jen-Inn Chyi
Dr. Wen-Hao Chang

Institute of Electrophysics
National Chiao Tung University

ABSTRACT

This dissertation is devoted to band structure engineering and device applications of GaAsSb-capped InAs Quantum Dots (QDs). In the first part of this dissertation, four approaches are utilized to tailor the band alignments of GaAsSb-capped InAs QDs. First, carrier dynamics of GaAsSb-capped InAs QDs with different Sb composition were investigated by time-resolved photoluminescence (TRPL). Both the power dependence of PL peak shift and the long decay time constants confirm the type-II band alignment at the heterointerface. Different recombination paths have been clarified by temperature dependent measurements. Second, we study the effects of thermal annealing on the emission properties of type-II GaAsSb-capped InAs QDs. Apart from large blueshifts and a pronounced narrowing of the QD emission peak, the annealing induced alloy intermixing also leads to enhanced radiative recombination rates and reduced localized states in the GaAsSb capping layer (CL). Evidences of the evolution from type-II to type-I band alignments are obtained from time-resolved and power-dependent PL measurements. The third approach is the modulation of the CL thickness. Both the emission energy and the recombination lifetime are found to be correlated with the CL thicknesses. Theoretical calculations indicate that the quantum confinement and the wave function distribution of hole states are sensitive to the GaAsSb CL thickness. The Sb induced change in QD size also plays a role in the optical properties of GaAsSb-capped QDs. The last approach is using the quaternary AlGaAsSb CL. As evidenced from power-dependent and time-resolved PL measurements, the GaAsSb-capped QDs with type-II band alignment can be changed to type-I by adding Al into the GaAsSb CL. The evolution of band alignment with the Al content in the AlGaAsSb CL has also been confirmed by theoretical calculations. The PL thermal stability and the room temperature PL efficiency are also improved by AlGaAsSb capping.

Device applications of GaAsSb-capped InAs QDs are demonstrated in the second part of this dissertation. First, spectral responses of GaAsSb-capped InAs/GaAs quantum-dot infrared photodetectors (QDIPs) with different Sb composition are investigated. Compared with the conventional InAs/GaAs QDIPs with wide detection windows, a much narrower

spectral width is observed for GaAsSb-capped QDIPs at longer detection wavelengths. The phenomenon is attributed to the larger InAs QDs with improved uniformity resulted from the GaAsSb CL. In this case, lowered energy states and reduced energy difference in-between would result in longer detection wavelengths with narrower spectral widths of GaAsSb-capped QDIPs. By comparing with photoluminescence excitation spectra of the samples, the dominant transition mechanisms for GaAsSb-capped QDIPs are also investigated. The other application is memory device. To further simplify the fabrication procedure, the architecture of wide-channel in-plane gate transistors (IPGTs) is adopted to demonstrate the memory effect of GaAsSb-capped InAs QDs. Hence, we studied IPGTs with an *n*-GaAs sheet resistance prior to the investigation of memory device. A trade-off between effective current modulation and high saturation drain current is obtained by optimizing the doping density of the sheet resistance. The mechanism responsible for the transistor behaviors of the devices is due to the channel electron depletion related to the population of mobile surface electrons under different gate biases. The photocurrent measurements demonstrate that the IPGT architecture is a feasible approach for the applications of photodetectors. After having the idea of the wide-channel IPGT, we demonstrate room-temperature electron charging/discharging phenomena of InAs QDs using wide-channel IPGTs. The device based on type-II GaAsSb-capped InAs QDs exhibits both the longer charging and discharging times than those of the type-I counterpart with GaAs CL. The slow charge relaxation of GaAsSb-capped InAs QDs and simple architecture of IPGT reveal the potential of this device architecture for practical memory applications.

CONTENTS

LIST OF FIGURES

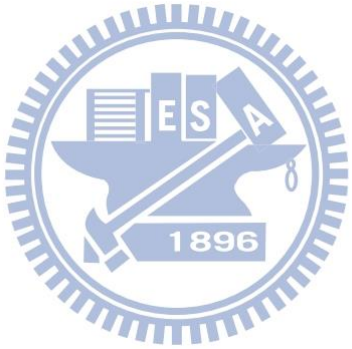

Chapter 1 General Introduction

1.1. OVERVIEW OF SELF-ASSEMBLED QUANTUM DOTS

Low-dimensional phenomena have been urgent and inevitable challenges toward the next generation semiconductor devices in the recent decades. Scaling down the dimensional of semiconductor structures not only saves space and increases the capacity of a single chip, but also brings the benefits of quantum effects. When the size of the material is reduced to the nanometer scale in one direction, the freedom of electron movement is lost in that direction. This confinement results in the quantization of the electron energy and in the variations of the electron density of states, which is the most remarkable and significant benefit of low-dimensional semiconductor technology. It has been considered that these quantization effects in a semiconductor structure can make an electronic device more efficient. For instance, Quantum wells, where electrons are confined in a plane, have been extensively utilized in our daily life. If material dimension are further reduced to restrict electrons in a small volume, quantum dots (QD) are formed. QDs are tiny semiconductor nanoparticles, which range from nanometers to tens of nanometers in size. With carrier confinement in three dimensions, the density-of-states of QDs are discrete, or so-called *ä*-function-like. The unique strongly size-dependent optical and electrical properties are differential to those of the corresponding bulk material. Furthermore, QDs are expected to have great potentials and advantages in several varieties of applications in optoelectronics.

Generally, semiconductor QDs can be manufactured by two main approaches. The first one is utilizing the lithography to pattern and etch the quantum well semiconductor structures.

The way is like to "*carve out*" QDs from bulk semiconductor materials. Although this conventional technique is convenient for mass-production of QDs, it is difficult to form QDs which are defect-free and exhibiting abrupt carrier confining potential. In addition, their high surface recombination rates due to the high surface-to-volume ratio, together with the damages introduced during the fabrication processes, significantly restrict them from optoelectronic applications. On the other hand, the other one is by mean of "*growing*" QDs from ad-atoms. It is the so-called self-assembled QDs [1,2] via heteroepitaxial growth in lattice-mismatched semiconductor system, such as typical In(Ga)As/GaAs and Ge/Si QDs which can be grown by using molecular beam epitaxy (MBE) or metal-organic chemical vapor deposition (MOCVD).

The formation of self-assembled QDs is by means of the self-assembled effects which are very common in strained semiconductor heterostructures. After Stranski and Krastanow first proposed the possibility of island formation on an initially flat heteroepitaxial surface in 1937, the growth of island formation on an initially two-dimensional (2D) layer by relaxing strain energy via misfit dislocations was generally referred to the Stranski-Krastanow growth mode (SK mode) [3]. In general, heteroepitaxial growth can be divided into three well-known modes depended on the interfacial surface energy and lattice mismatch [4]. They are Frank-van der Merwe (FvdM mode) [5], Volmer-Weber (VW mode) [6], and Stranski-Krastanow (SK mode) [3], which are schematically depicted in Fig. 1.1. For FvdM mode, it occurs in lattice-matched material systems and is commonly referred to as layer-by-layer growth mode. The deposited material wets the substrate when the surface energy of deposited material is lower than that of the substrate. On the contrary, when the surface energy of deposited material is larger, direct formation of three-dimensional (3D) islands will take place to minimize the system total energy, leading to the VW mode. The SK mode takes place in a lattice-mismatched system with small surface energy. Layer-by-layer growth is expected at the initial stage of growths. With the increasing amount of deposited

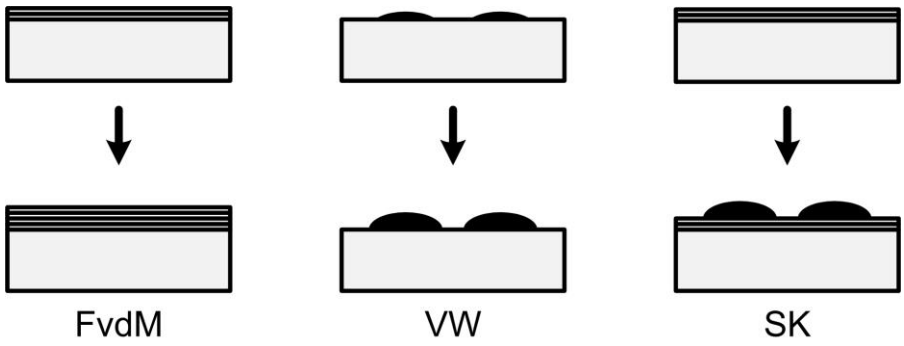

Fig. 1.1: Heteroepitaxial growth modes: Frank-van der Merwe (FvdM), Volmer-Weber (VW), and Stranski-Krastanow (SK).

material, the accumulated strain energy is getting larger. To release the strain energy, a transformation from the initially 2D growth to a 3D island growth occurs and the initial 2D layer underneath the islands is named "*wetting layer*".

As far as the mechanism of strain relaxation, it was believed to occur not only through the formation of islands, but accompany the formation of misfit dislocations underneath. Some literatures have demonstrated the formation of coherently 3D strained islands without defect generations on InGaAs/GaAs system [7] and on Si/Ge system [4]. Since the elastic-deformation mechanism contributes to the lattice of the substrate approach to the strained island, the total strain energy can thus be lowered without introducing misfit dislocations. If the amount of deposited material were further increased, deformation of the substrate lattice will become unstable, leading to a transition of coherent SK islands back to the dislocated SK islands.

Relevant works are devoted to the optimized growth conditions in In(Ga)As/GaAs system [8-11]. The formed strained In(Ga)As islands are self-assembled with superior uniform size and shape distributions. The typical island revealed a favorable size with a

lateral dimension of 15~25 nm and a height of 3~5 nm. After the wide-band gap GaAs overgrowth, the islands behave like a *quantum dot*, which confines both the electron and the hole three-dimensionally by its surrounding GaAs of wider band gap, thus exhibiting atomic-like properties.

Accomplishments in acquiring high-quality and defect-free QDs not only open the door to the fundamental low-dimensional studies, but also stimulate developments of their applications in optoelectronic devices. One of the valuable applications is quantum-dot lasers. Relevant works were devoted to the development of quantum-dot lasers since Arakawa and Sakaki predicted quantum-dot lasers should have superior characteristics, such as ultra-low threshold, less temperature-dependence, and enhanced differential gain [12]. This is primarily because, as the dimension of materials is reduced, the density of state for electrons changes to give a narrower optical transition spectrum, making the light-matter interaction more efficient. The first demonstration of quantum-dot laser was reported by Kirstaedter *et al*. in 1994[13,14]. Improved operation by increasing the density of QDs was achieved by Bimberg *et al*. in 1996 [15]. They also enabled high-power continuous-wave laser operations [16] by stacking the QDs vertically which can achieve vertical coupling of the QDs [17].

Besides the applications in optical devices, self-assembled QDs have also been proposed for memory device applications. The read/write process in QD memory devices require low operation voltage since tunneling is employed for carrier injection and depletion [18]. With other advantages of high read/write speed, enhanced carrier storage capacity, and better endurance, QD memory devices are more reliable in comparison to other nonvolatile memory devices [19,20]. Lots of efforts have been devoted to the investigations of memory characteristics of InAs/GaAs QDs based on optically [21,22] and electrically [23-28] carrier injections. Room-temperature (RT) memory operations have also been demonstrated by using multi-stacked QD layers [22,23] and an optimized positioning of a single InAs QD layer in a local conduction band minimum [25].

More recently, a novel QD application of the intermediate-band solar cells (IBSC) has attracted much attention [29-31]. The concept is forming a mini-band in the active region of the solar cell. Thus, photons with sub-band gap energies can excite electrons to the continuum above the conduction band in a two-step process through the intermediate band, leading to a significant increase in the solar energy conversion efficiency. The QDs are ideal candidate for the creation of the intermediate band by composing of the ground states in close-stacked QDs. Within this framework, a limiting efficiency of 63.2% has been predicted for the IBSC, compared to 40.7% for conventional single gap solar cells [29]. The critical issue is their limited contribution to the total photocurrent due to the small volume of the QDs, so stacks of tens of QD layers are usually needed. However, it is well known to also increase the accumulated stress of the material during growth, generating dislocations and non-radiative recombination centers. Many efforts have dedicated to overcome the challenge, including introducing strain compensation layers [32,33].

Although varieties of applications of self-assembled QDs were successful demonstrated, these device are still far from the demands of commercial markets. The major problem is that QDs size uniformity is still not good enough. Besides, site-controlled QDs is an issue for other specific applications as well.

1.2. IMPACTS OF THE GAASSB CAPPING LAYER ON THE UNDERLYING SELF-ASSEMBLED INAS QUANTUM DOTS

Self-assembled InAs QDs grown by MBE have been extensively investigated, relying on its mature development in the growth technique. However, the nature of self-assembled QD growth procedure makes it difficult to manipulate QD morphologies and the corresponding device performances such as detection wavelength tuning and inter-band emitting wavelength extending. To overcome this problem, one of the most straightforward solutions is the change of capping layer (CL) over InAs QDs from GaAs to different materials. In this case, similar QD morphologies can still be maintained while the band structures of InAs QDs with different CLs can be altered. Self-assembled InAs QDs with a GaAsSb CL have attracted much attention recently in the study of improving the performance of long-wavelength QD-based devices [34-37]. It has been reported that the impacts of the GaAsSb CL on the underlying InAs QDs are manifold. First, similar to the conventional InGaAs CL, the GaAsSb CL acts as a strain reducing layer for the QDs [38] and has great capability of tuning the emission wavelength towards 1.5 μm or beyond for telecommunication applications. Emission wavelength beyond 1.5 μm and RT continuous-wave operation of a 1.3 μm QD laser have been demonstrated. Second, the presence of Sb atoms in the CL is also helpful for suppressing the QD decomposition [39,40]. Typical GaAs-capped InAs QDs exhibit a truncated pyramid shape of about 4 nm due to strong Indium redistribution and/or out-diffusion during the capping processes, while that with the GaAsSb CL are lens-shaped with a height of about 8 nm. The enlargement in QD height improves carrier confinement and reduces the sensitivity of the excitonic band gap to QD size fluctuation within the ensemble. It has been shown that both effects can lead to a redshifted emission wavelength, an improved

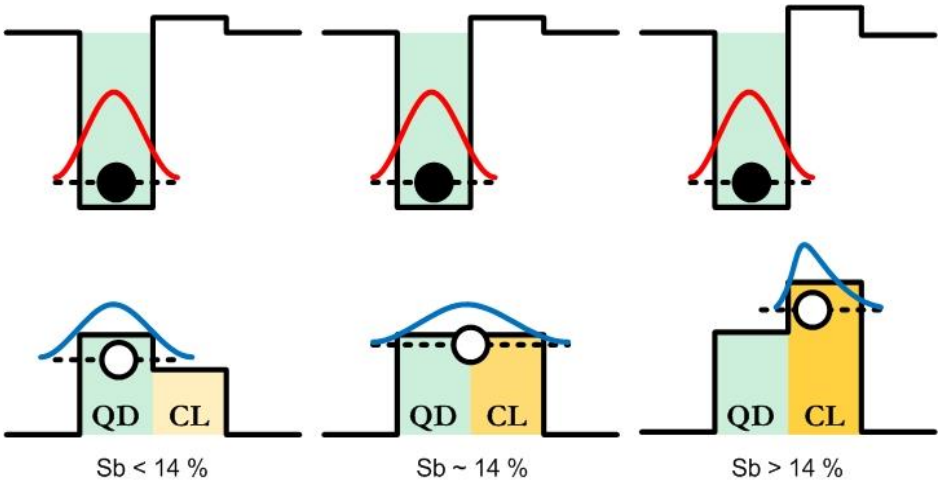

Fig. 1.2: Schematic band diagrams of InAs QDs with $GaAs_{1-x}Sb_x$ CLs.

photoluminescence (PL) efficiency, and a narrower spectral width for Sb content less than 12-14%. The third and the most prominent effect is the large valence band (VB) offset at the InAs-GaAsSb heterointerface, which is beneficial to promote holes thermal stability. Schematic band diagrams of InAs QDs with the $GaAs_{1-x}Sb_x$ CL are shown in the Fig. 1.2. When Sb content exceeds ~14 %, the heterostructure transforms from a type-I band alignment to a type-II band alignment [41,42].

Experimental evidences for the type-II QDs have been reported based on power-dependent PL and time-resolved PL (TRPL) measurements. Due to the spatial separation of electrons in the QDs and holes in the GaAsSb CL, the carrier lifetime should be much longer than their counterparts (i.e., InAs/GaAs QDs). Although such spatially indirect excitons with long carrier lifetimes [43,44] and the confinement of only one carrier species make the QDs very promising for memory [19] and photovoltaic devices [31,45], the degraded recombination efficiency is however detrimental for light emitting devices and laser applications. In addition, it has been pointed out that VB discontinuity plays an important role

in the design of multiple transition solar cells [46]. The use of antimony in the CL could have a strong advantage in obtaining a negligible VB offset, which is thought to be one of the key challenges in the development of QD-based solar cells. Hence, tailoring the transition energy, the band alignment, the wave function overlaps, and hence the carrier dynamics are desirable for specific applications. Several works have been devoted to achieve the goal, such as varying the Sb composition in the GaAsSb CL [40,41], post-growth thermal treatments [47,48], varying the GaAsSb CL thickness [49], graded Sb content in CL [50], or using quaternary GaAsNSb [51], InGaAsSb [52] and AlGaAsSb [53] CLs.

1.3. OUTLINE OF THIS DISSERTATION

The dissertation is devoted to optical properties and device applications of self-assembled InAs QDs with a GaAsSb CL. Before discussing the physics of the materials and the characteristics of the devices, an overview of self-assembled QDs and effects of the GaAsSb CL on the underlying self-assembled QDs are introduced in Chapter 1.

The keynote of Chapter 2 is the band alignment engineering of InAs QDs with a GaAsSb CL. We present four approaches to achieve the goal including varying the Sb composition in the CL, post-growth thermal treatments, thickness modulation of the CL, and quaternary AlGaAsSb CL. Varying the Sb composition in the CL, the most straightforward strategy, is discussed in Sec. 2.1. Carrier dynamics of InAs QDs with a $GaAs_{1-x}Sb_x$ CL were investigated by TRPL. Besides confirming the type-II band alignment at the GaAsS-InAs interface from both the power dependence of PL peak shift and the longer decay time constants, different recombination paths have been clarified by temperature dependent measurements. Another alternative approach is the use of post-growth thermal annealing to smooth the VB discontinuity by the annealing induced alloy intermixing. In Sec. 2.2, we employed PL and TRPL spectroscopes to investigate the emission properties of the GaAsSb-capped InAs QDs after thermal annealing at temperatures ranging from 700 to 900 ^{o}C. The annealing induced changes in the band alignment, the carrier dynamics and electronics structures due to the alloy intermixing were observed and discussed. In Sec. 2.3, we investigate the evolutions of emission energy and recombination lifetime of the GaAsSb-capped InAs QDs with the CL thickness. The effects of the CL thickness on the hole states and their wave function distributions are discussed and compared with theoretical calculations. For applications in long-wavelength light emitters, we demonstrate the tuning of band alignment and optical properties of InAs/GaAs QDs using a thin quaternary AlGaAsSb

CL in Sec. 2.4. As evidenced from power-dependent PL and TRPL measurements, the GaAsSb-capped QDs with type-II band alignment can be changed to type-I by adding Al into the GaAsSb CL. The evolution of band alignment with the Al content in the AlGaAsSb CL is also compared with theoretical calculations.

Following the idea of band alignment engineering and optical properties of GaAsSb-capped InAs QDs, the practical device applications are demonstrated in Chapter 3. Spectral responses of GaAsSb-capped InAs/GaAs quantum-dot infrared photodetectors (QDIPs) with different Sb composition are investigated in Sec. 3.1. By comparing with photoluminescence excitation (PLE) spectra of the samples, the dominant transition mechanisms for GaAsSb-capped QDIPs are also investigated. The narrow spectral width of the device is advantageous for selective detections at specific wavelengths for QDIPs. Another potential application of the type-II GaAsSb-capped InAs QDs is memory device. To further simplify the fabrication procedure, in-plane gate transistors (IPGTs) with micrometer-sized channel widths are adopted to demonstrate the memory effect of GaAsSb-capped InAs QDs. An IPGT with *n*-GaAs sheet resistance is investigated in Sec. 3.2. The photocurrent measurements demonstrate that the architecture is a feasible approach for the applications of photodetectors and the mechanism responsible for the transistor behaviors of the devices is also discussed. After having the ideas of IPGTs, we investigate room-temperature electron charging/discharging behaviors of InAs QD using IPGTs in Sec.3.3. The slow charge relaxation of GaAsSb-capped InAs QDs and simple architecture of IPGT reveal the potential of this device architecture for practical memory applications.

Finally, we summarized the conclusions of these studies in Chapter 4.

Chapter 2 Band Structure Engineering in GaAsSb-Capped InAs Quantum Dots

2.1. VARYING THE ANTIMONY COMPOSITION

The most straightforward strategy in tailoring the band alignment of InAs QDs with a GaAsSb CL is directly varying the Sb composition in the CL. It has been believed to exhibit a type-II band alignment when the Sb composition exceeds over 14%. Experimental evidences for the type-II transition have been reported based on power dependent PL measurements [41,42]. However, relevant reports regarding TRPL have been rare so far [43], which would provide a more direct evidence on the nature of radiative recombination in such type-II QDs.

In this section, we report a TRPL study on the GaAsSb covered InAs QDs. The much longer decay time confirms a type-II band lineup at the GaAsSb–InAs interface. Different recombination paths were discussed and identified by temperature dependent measurements.

2.1.1 Experimental details

The samples investigated in this section were grown on GaAs substrates by MBE. After the growth of a 200 nm thick GaAs buffer layer, a layer of InAs QD (2.7 ML, monolayer) was grown at 500 ℃ and subsequently capped by a 4.5 nm $GaAs_{1-x}Sb_x$ layer. Two samples with nominal x of 16% and 21% were prepared. A sample with GaAs covered InAs QDs (x=0%) was also grown as a reference of type-I QDs. All samples were finally capped by a 50 nm GaAs layer. Atomic force microscopy of uncapped samples reveals that the QDs are lens

shaped, with an average height of ≈8±0.5 nm, a diameter of ≈20 nm, and a density of 3×10^{10} cm^{-2}. PL was excited by an argon ion laser (488 nm), analyzed by a 0.5 m monochromator and detected by an InGaAs photomultiplier tube. TRPL was performed using either a 200 fs Ti:sapphire laser (780 nm/80 MHz) or a 50 ps pulsed laser diode (405 nm/5 MHz). The decay traces were recorded using the time-correlated single photon counting technique with an overall time resolution of ~150 ps.

2.1.2 Optical properties

Figure 2.1 shows the PL spectra for the QD samples with different Sb compositions. A redshift in peak energy was observed with the increasing *x*. The power dependent PL spectra for the 16% sample are displayed in Fig. 2.2(a). Increasing the excitation power (P_{ex}) results

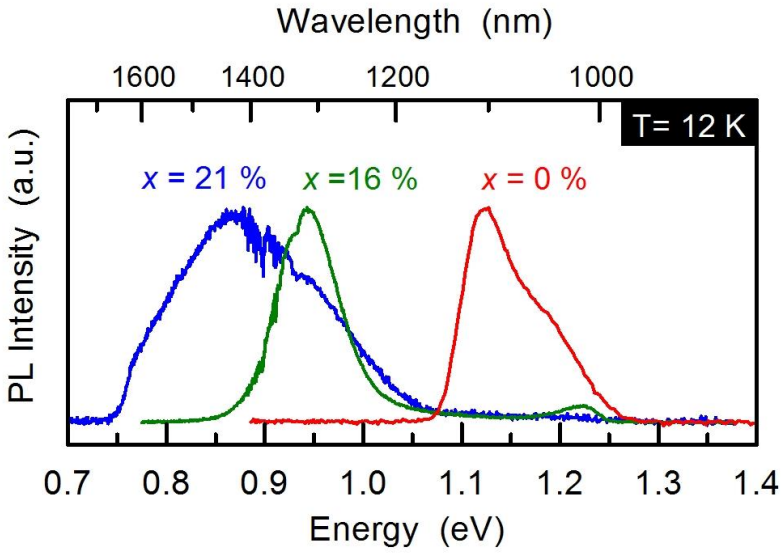

Fig. 2.1: PL spectra of the $GaAs_{1-x}Sb_x$ capped InAs QDs with different *x*.

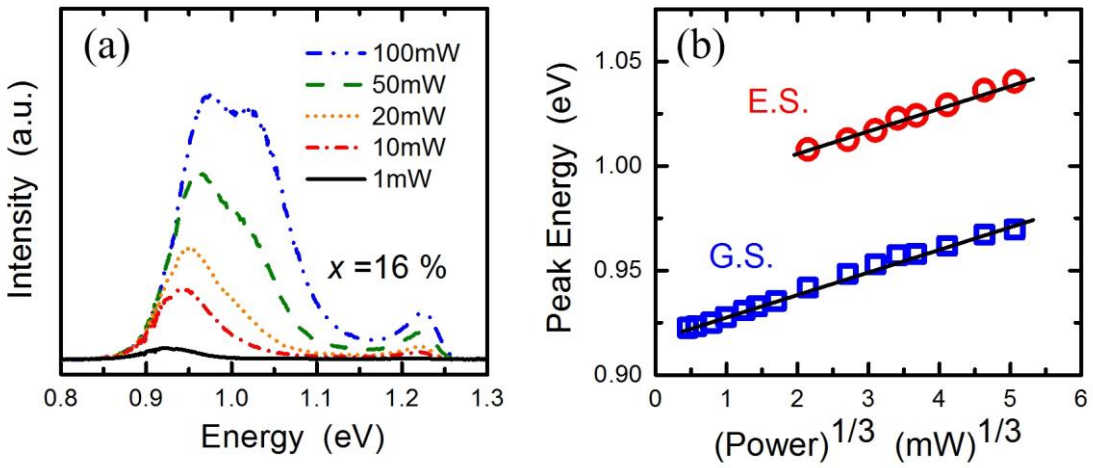

Fig. 2.2: (a) Power dependent PL spectra of the 16% sample. (b) The GS and the ES peak energies as a function of $P_{ex}^{1/3}$ for the 16% sample.

in a blueshift in QD emission peaks. The energy shift shows a linear dependence on $P_{ex}^{1/3}$ [see Fig. 2.2(b)], consistent with the behavior expected for a type-II band alignment [42,54]. The PL peak can thus be identified as the recombination of ground-state (GS) electrons in the QDs with holes in the GaAsSb layer confined by the field induced band bending surrounding the QDs. The QD excited state (ES) appeared under higher P_{ex}'s. A similar power dependence of the blueshift was also observed for the QD ES.

Figure 2.3 shows the TRPL of the investigated samples measured at T =12 K. The decay time for the reference InAs/GaAs QDs was $\tau \approx 0.8 \pm 0.2$ ns, comparable with the reported typical value of ~1 ns [55]. In contrast, the GaAsSb covered QDs exhibit much longer decay times than the reference InAs QDs. This can be attributed to the reduced spatial overlap between the electron and hole wavefunctions due to the type-II band alignment [56]. We notice that the decay traces for the GaAsSb covered QDs are non-single-exponential,

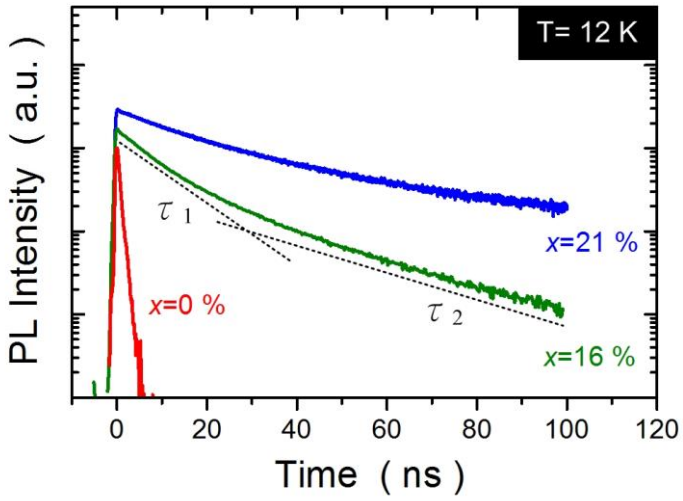

Fig. 2.3: TRPL decay traces for the $GaAs_{1-x}Sb_x$ capped InAs QDs with different *x*.

which can be decomposed into a faster initial component and a slower tail component. In order to obtain decay time constants, they are fitted by a double exponential function:

$$I(t) = A_1 e^{-t/\tau_1} + A_2 e^{-t/\tau_2}$$

For the 16% sample, the deduced time constants are τ_1=7.5 ns and τ_2=24 ns, with a relative ratio of A_2/A_1=0.4. The time constants for the 21% sample are somewhat longer ($\tau_1 \approx$ 8.2 ns and $\tau_2 \approx$ 29 ns), with a more pronounced slower decay component ($A_2/A_1 \approx$ 0.5).

Similar non-single-exponential decays have been observed in GaSb/GaAs type-II QDs [57,58]. A quite general picture considering a time-dependent recombination rate of nonequilibrium carriers has been established and the schematic illustration is shown in Fig. 2.4. For the GaAsSb covered InAs/GaAs QDs investigated here, the underlying processes can be understood as follows. After the carrier excitations, electrons are captured rapidly into the QDs, exhibiting a band bending in the surrounding. On the other hand, holes are captured into

the GaAsSb quantum well (QW) and then attracted by the nonequilibrium electrons. The induced band bending tends to confine the hole closer to the QDs and hence increases the electron-hole wavefunction overlap. The faster initial decay time τ_1 can thus be related to the *short-range* radiative recombination of the QD electrons with the holes confined in the surrounding band bending. As the nonequilibrium electrons recombine continuously, the band bending reduces, leading to a reduced wavefunction overlap and hence a lower recombination rate. The band-bending effect would eventually become negligible when most of the nonequilibrium carriers have recombined. The longer decay time τ_2 thus reflects the *long-range* radiative recombination of the QD electrons with the holes in the GaAsSb QW states.

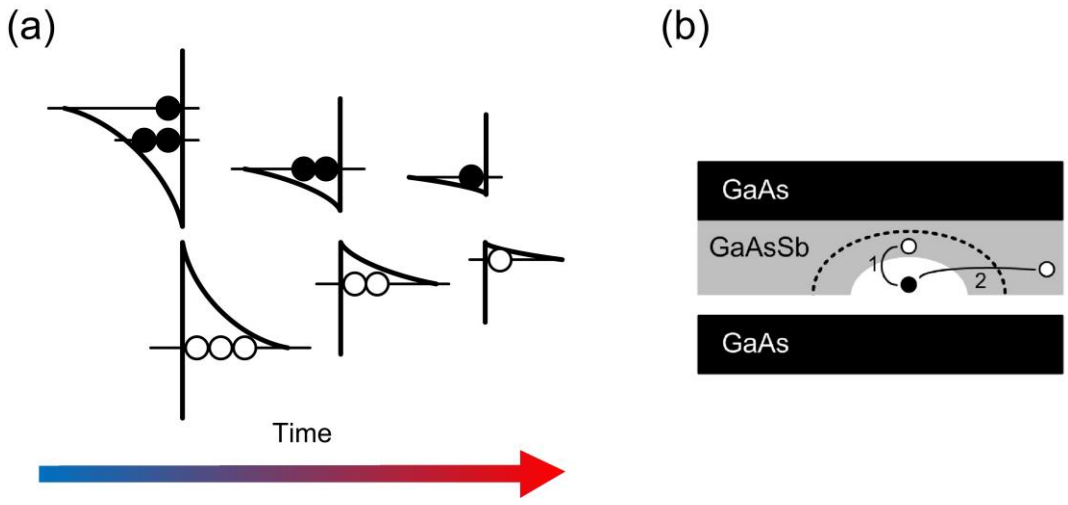

Fig. 2.4: (a) The schematic illustration of a time-dependent recombination rate of non-equilibrium carriers. (b) The sample structure and the underlying recombination processes responsible for the faster (1) and the slower (2) decay components.

2.1.3 Temperature-dependent measurements

As elucidated above, the effect of nonequilibrium carriers is expected to be negligible under lower excitation conditions [57]. However, we found that the PL decay traces are still non-single-exponential even though the initial carrier density N_0 was reduced to less than 1 electron/dot. To further clarify this point, temperature dependent TRPL has been performed. The results for the x=16% sample are displayed in Fig. 2.5. In this study, the P_{ex} was kept low so that only the GS peak was observed (i.e., $N_0 \lesssim 2$ electrons/dot). We found that the PL peak exhibits a so-called *S*-shaped energy shift with the temperature. This is a

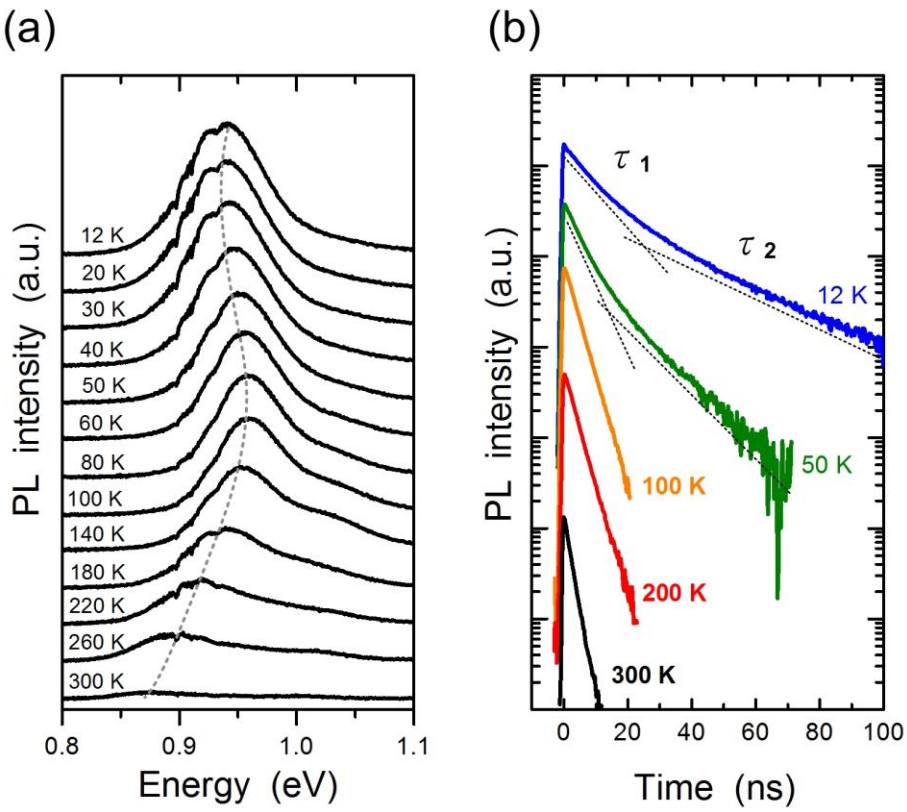

Fig. 2.5: Temperature evolution of the PL spectra (a) and decay traces (b) for the x=16% sample.

typical feature of carrier localization effect and has already been observed in many alloy systems, such as InGaN/GaN and GaInNAs/GaAs QWs [59,60]. Because no *S*-shaped feature was observed in the reference InAs/GaAs QDs, the carrier localization must be in the GaAsSb CL, due possibly to alloy fluctuations and/or Sb clustering.

By comparing the *S*-shaped feature with the temperature dependent decay traces, the carrier dynamics of the non-single-exponential decay become clear. As shown in Fig. 2.5(b), the slower decay component was observed only at T<100 K. Because photogenerated holes are trapped by the localization states in the GaAsSb QW at low temperatures, they are less mobile and unable to be attracted into the bend-bending region induced by the QD electrons. This explains why the slower decay component can be observed at T<100 K even under low excitation conditions. With the increasing T from 30 to 100 K, these trapped holes gain thermal energy and start to populate the two-dimensional (2D) state of the GaAsSb QW. As the temperature was further increased, most of the holes were delocalized to the 2D QW state and hence could be efficiently attracted into the bend-bending region. Accordingly, the decay traces exhibit a well-defined single decay time constant τ_1 at $T\gtrsim$100 K, as expected for low excitation conditions.

Quantitatively, the hole localization energy can be deduced from the *S*-shaped energy shift. By using the relation combining the Varshni equation and localization effect [61],

$$E(T) = E(0) - \frac{\sigma^2}{kT} - \frac{\alpha T^2}{(\beta + T)}$$

, with parameters E_0=0.998 eV, α=11×10^{-4} eV/K, β=600 K, and a localization energy $\sigma\approx$14 meV, a reasonable fit can be obtained [solid line in Fig. 2.6(a)]. An Arrhenius plot of the time-integrated intensities of the faster ($I_1 = A_1\tau_1$) and the slower ($I_2 = A_2\tau_2$) decay components obtained from the TRPL traces is shown in Fig. 2.6(b). In the range of T=30–100 K (the shadow region), I_2 decreases while I_1 increases in such a way that the total intensity

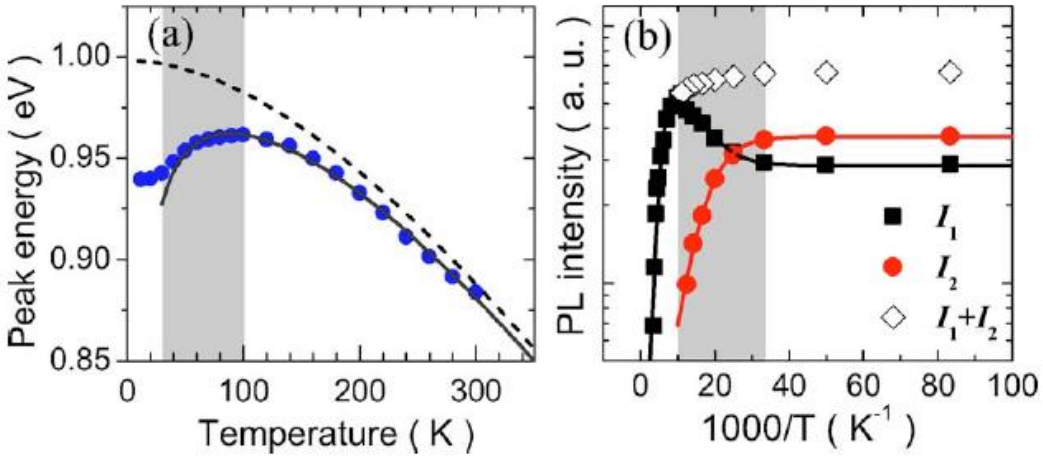

Fig. 2.6: (a) The PL peak energy as a function T. Lines are fitting curves with (solid) and without (dashed) localization effects. (b) An Arrhenius plot of the time-integrated intensities for the faster (I_1) and the slower (I_2) decay components.

I_1+I_2 remains nearly constant. Such intensity changes clearly elucidate the carrier transfer process: the trapped holes are gradually delocalized by thermal energy and attracted into the bend-bending region surrounding the QDs. The activation energy for I_2 was found to be E_A≈18 meV, close to the deduced localization energy σ. For T≳100 K, the faster time constant is τ_1 =3.3±0.4 ns and is insensitive to T, as expected for well-confined zero-dimensional carriers. The time constant[1] is approximately four times longer than the reference InAs QDs, corresponding to an electron-hole wavefunction overlap of ~50% of the type-I QDs. This value is considerably larger than that expected for a type-II exciton [56]. The appreciable overlap may be enhanced by the quantum confinement of the GaAsSb/GaAs QW. In addition, the small band discontinuity between InAs and $GaAs_{0.84}Sb_{0.16}$ is also responsible for such an appreciable overlap.

[1] The measured τ_1 at T~100 K can be approximated as the actual recombination lifetime because both the temporal PL shift caused by the nonequilibrium electrons and the hole localization effect are less significant. For T>200 K, however, the rapid decrease in the integrated PL intensity indicates that the nonradiative processes are increasingly important.

In summary, carrier dynamics of type-II InAs/GaAs QDs covered by a thin GaAsSb layer have been investigated by TRPL measurements. Different recombination paths in such type-II QDs have been clarified by temperature dependent measurements. The long-range recombination with the holes trapped by localized states in the GaAsSb QW is significant at low temperatures. At higher temperatures, the recombination is dominated by the holes confined to the band bending region surrounding the QDs.

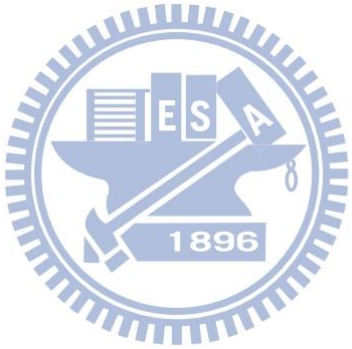

2.2. RAPID THERMAL ANNEALING

Tailoring of the band alignment, the wave function overlaps and hence the carrier dynamics in InAs/$GaAs_{1-x}Sb_x$ QDs is necessary for practical applications. In particular, it has been pointed out that the VB discontinuity plays an important role in the design of multiple transition solar cells. The use of antimony in the CL could have a strong advantage in obtaining a negligible VB offset, which is thought to be one of the key challenges in the development of QD-based solar cells. In principle, this can be done by varying the Sb composition in the $GaAs_{1-x}Sb_x$ layer to change the VB discontinuity at the InAs- $GaAs_{1-x}Sb_x$ interface. However, alloy fluctuations and Sb clustering were usually accompanied with the increasing Sb content, making the QD's optical properties even hard to control. An alternative approach is the use of postgrowth thermal annealing to smooth the VB discontinuity at the InAs/$GaAs_{1-x}Sb_x$ interface by the annealing induced alloy intermixing.

In this section, we employed PL and TRPL spectroscopes to investigate the emission properties of the InAs/$GaAs_{1-x}Sb_x$ type-II QDs after thermal annealing at temperatures ranging from 700 to 900 ℃. The annealing induced changes in the band alignment, the carrier dynamics, and electronics structures due to the alloy intermixing were observed and discussed.

2.2.1 Experimental details

Self-assembled InAs QDs were grown by MBE on GaAs substrates. The type-II QDs were formed by depositing 2.7 ML of InAs on a 200 nm thick GaAs buffer layer at 500 ℃ and subsequently capped by a 4.5 nm $GaAs_{1-x}Sb_x$ layer with a nominal x=0.16. A sample with GaAs covered InAs QDs was also grown as a reference of type-I QDs. Atomic force microscopy of uncapped samples reveals that the QDs are lens shaped, with an average height of ≈8±0.5 nm, a diameter of ≈20 nm, and a density of 3×10^{10} cm^{-2}. Finally, the QDs

were capped by a 50 nm GaAs layer. Postgrowth rapid thermal annealing for the GaAsSb covered sample was performed at annealing temperatures T_A ranging from 700 to 900 ℃ for 20 s using GaAs proximity capping.

2.2.2 Effects of thermal annealing on the emission properties

Figure 2.7(a) shows the PL spectra for the as-grown and the annealed QD samples measured at 10 K under a low excitation power of 0.5 mW. The PL spectrum for the type-I InAs/GaAs QDs is also shown for comparison. With the increasing T_A, a blueshift and a

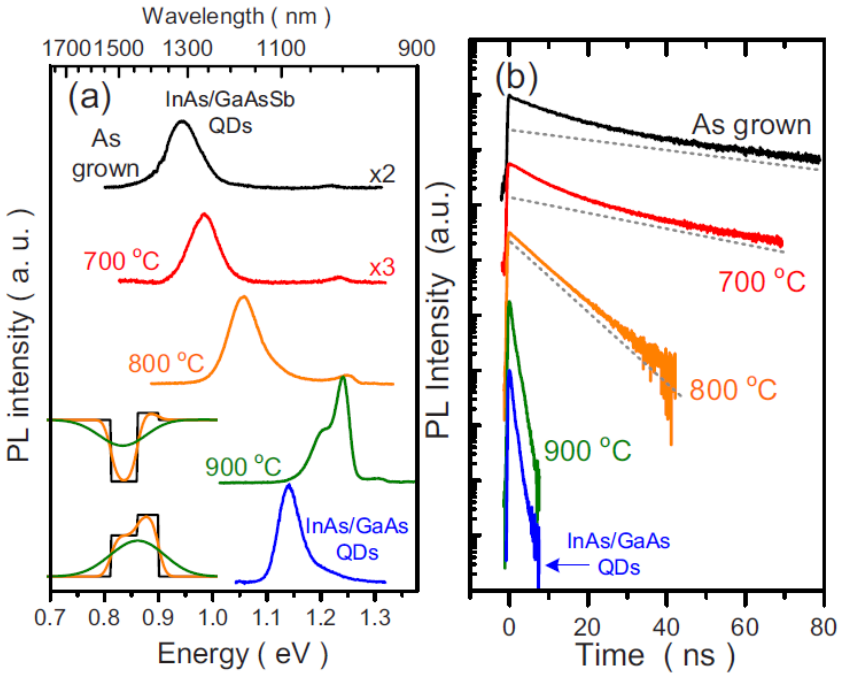

Fig. 2.7: PL spectra (a) and TRPL decay traces (b) for the as-grown and annealed InAs/GaAsSb QDs, together with the reference InAs/GaAs QDs.

narrowing of the QD's emission peak were observed [62-67]. The energy blueshift is caused by the alloy intermixing between the QDs and barrier materials, which shallows the QD's confining potential due to the incorporation of more Ga atoms into the InAs QDs [62-67]. For the as-grown sample, it has been confirmed in our previous study (Sec. 1 in this chapter) that the InAs/$GaAs_{0.84}Sb_{0.16}$ QDs exhibited a type-II band lineup, where the radiative recombination occurs between the electrons confined in the QDs and the holes in the GaAsSb layer. Annealing induced alloy intermixing also tends to smooth the VB discontinuity at the InAs–GaAsSb interface. Therefore, the electron-hole wave function overlaps and hence the radiative recombination rate is expected to be enhanced or even changed gradually to type-I transitions after thermal annealing.

To understand the effects of thermal annealing on the recombination dynamics in the type-II QDs, TRPL measurements have been performed and the results are shown in Fig. 2.7(b). The PL decay time was found to decrease with the increasing T_A, indicative of a more penetrated hole wavefunction into the InAs QDs due to the reduced VB offset caused by alloy intermixing at the InAs–GaAsSb interface. In particular, we found that the decay transient for the 900 ℃ annealed QDs became as fast as the InAs/GaAs type-I QDs. This implies that the QD structure has been changed to a type-I band alignment after high-temperature annealing.

In principle, the recombination lifetime can be quantitatively deduced from the measured PL decay transients. However, the determination of recombination lifetime is not straightforward for a type-II system. One complication arises from the effect of nonequilibrium carriers: as the carriers recombine continuously, the PL shifts to lower energies due to the reduced VB bending surrounding the QDs. Therefore, the decay transient recorded at a given wavelength does not reflect the true lifetime since the PL decay arises not only from the carrier recombination but also from the temporal PL shift. For the InAs/GaAsSb material system, the carrier dynamics is further complicated by the presence of

localized hole states in the GaAsSb layer due to alloy fluctuations and/or Sb clustering. The redistribution of holes among these localized states also significantly influences the overall carrier dynamics, particularly at low temperatures. In order to clarify the role of both effects (i.e., the nonequilibrium carriers and the localized states) in the PL transients, energy dependent TRPL has been performed. The results for the 700 and 800 ℃ annealed QDs are shown in Figs. 2.8(a) and 2.8(b), respectively. For the 700 ℃ annealed QDs, a clear temporal PL redshift can be observed. Since the excitation power was kept low, the effect of

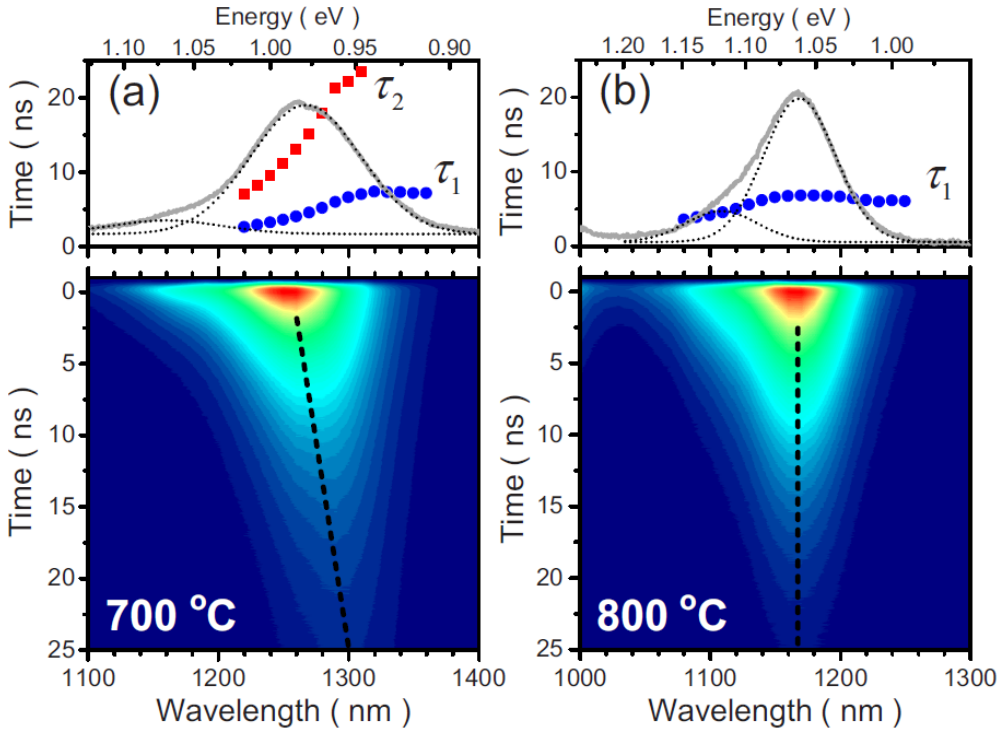

Fig. 2.8: Energy dependent carrier lifetimes and time evolution of the PL spectra for the samples annealed at (a) 700 ℃ and at (b) 800 ℃.

nonequilibrium carriers is expected to be less significant. In fact, an even more pronounced temporal PL shift was observed for the as-grown sample. Thus we ascribe the temporal PL redshift to the effect of hole localizations in the GaAsSb layer. On the contrary, the temporal PL redshift was absent for those QDs annealed at T_A≥800 ℃. This indicates that the localized hole states have been removed by the annealing induced alloy intermixing. The temporal PL redshift is closely related to the nonsingle exponential decay observed in PL transients shown in Fig. 2.7(b). Investigations of all samples revealed that the temporal PL redshift can be observed only when the decay transient is nonsingle exponential. By using a double exponential function $I(t) = A_1 e^{-t/\tau_1} + A_2 e^{-t/\tau_2}$ to fit the PL decay recorded at each wavelength, the decay time constants τ_1 and τ_2 for the faster and the slower decay components can be obtained. The fitted results are shown in the upper panel of Fig. 2.8, along with its time integrated PL spectrum. For the 700 ℃ annealed QDs, both τ_1 and τ_2 show strong energy dependences, indicative of hole transfers among localized states in the GaAsSb layer. For the 800 ℃ annealed QDs, we found that τ_1 is almost unchanged across the ground state emission band.

The energy dependent lifetime can be described by

$$\tau(E) = \frac{\tau_{rad}}{1 + e^{\frac{E - E_{me}}{E_0}}}$$

, where τ_{rad} is the radiative lifetime, E_0 describes the localization depth, and E_{me} is the energy similar to the mobility edge [68]. The schematic illustration of hole redistribution among fluctuant potentials and the corresponding energy dependent lifetime are shown in Fig. 2.9. As shown in the figure, carriers in shallower potentials are with higher probability of transfers, thus, resulting in shorter lifetimes. On the other hand, carriers in deeper potentials tend to recombine and the measured lifetimes are closer to radiative lifetimes.

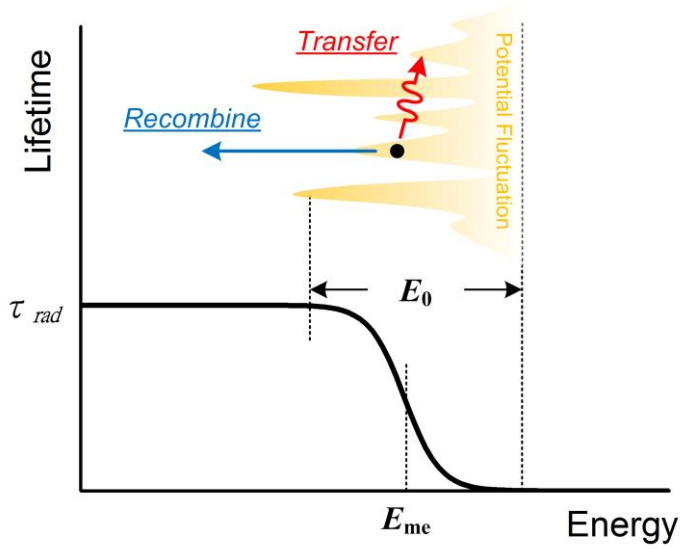

Fig. 2.9: The schematic illustration of hole redistribution among fluctuant potentials and the corresponding energy dependent lifetime.

Figure 2.10 shows the radiative recombination rate (τ_{rad}^{-1}) deduced from the energy dependent lifetime for all annealed samples. The measured τ_{rad} increases slightly from 0.095 ns^{-1} for the as-grown sample to 0.15 ns^{-1} after annealing at T_A=800 ℃, but still about an order of magnitude lower than the InAs/GaAs type-I QDs (1.25 ns^{-1}). The low recombination rates indicate that their band lineups remain type-II, with an electron hole wave function overlap of only ~28%–35% of the type-I QDs. As T_A was increased to 900 ℃, the recombination rate increases dramatically to τ_{rad}=1.2 ns^{-1}, which is very close to that of the type-I QDs, and confirms the band alignment change after annealing.

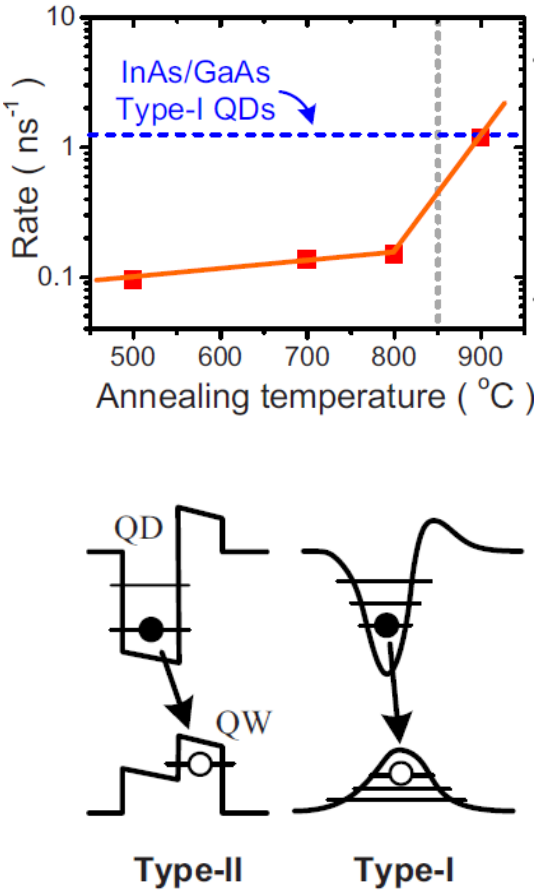

Fig. 2.10: Radiative recombination rate as a function of the annealing temperature. The data from the as-grown sample are plotted at 500 ℃.

2.2.3 The evolution of band alignments

In order to examine whether the QDs are still present after high-temperature annealing, rather than evolving into a quantum-well-like structure, we have also measured the power-dependent PL spectra for the annealed samples. Figure 2.11 shows a comparison among the power-dependent spectra for the QDs annealed at 700, 800, and 900 ℃. With the increasing excitation power (P_{ex}), higher energy peaks become observable for all samples due to the state-filling effect, which is a feature specific to a zero-dimensional system [63,65-67]. This demonstrates unambiguously that the annealed structures remain as QDs even after 900 ℃ annealing. The peak energy shifts in the power-dependent spectra also provide evidences for the band alignment changes after thermal annealing. For the 700 ℃ annealed QDs, the QD peaks shift linearly with $P_{ex}^{1/3}$, i.e., a fingerprint of type-II transitions. This feature is not observed for the QDs annealed at 900 ℃, confirming their type-I alignment. The most interesting is the case annealed at 800 ℃, where the peak blueshift is observed at lower excitation powers but becomes nearly unchanged for P_{ex}>5 mW. This behavior can be explained by an evolution from the type-II to type-I recombination induced by the large VB bending surrounding the QDs. After 800 ℃ annealing, the VB offset at the InAs-GaAsSb interface has been reduced by the alloy intermixing. To confine holes around the QDs and retain a type-II recombination, the VB bending should be weak and the excitation power must be low. When a large amount of nonequilibrium electrons was injected into the QDs by a higher P_{ex}, a very strong VB bending will exhibit in the QD surrounding. This makes the small VB offset unable to support confined hole states in the QD surrounding, leading to a gradual evolution from a type-II to a type-I transition.

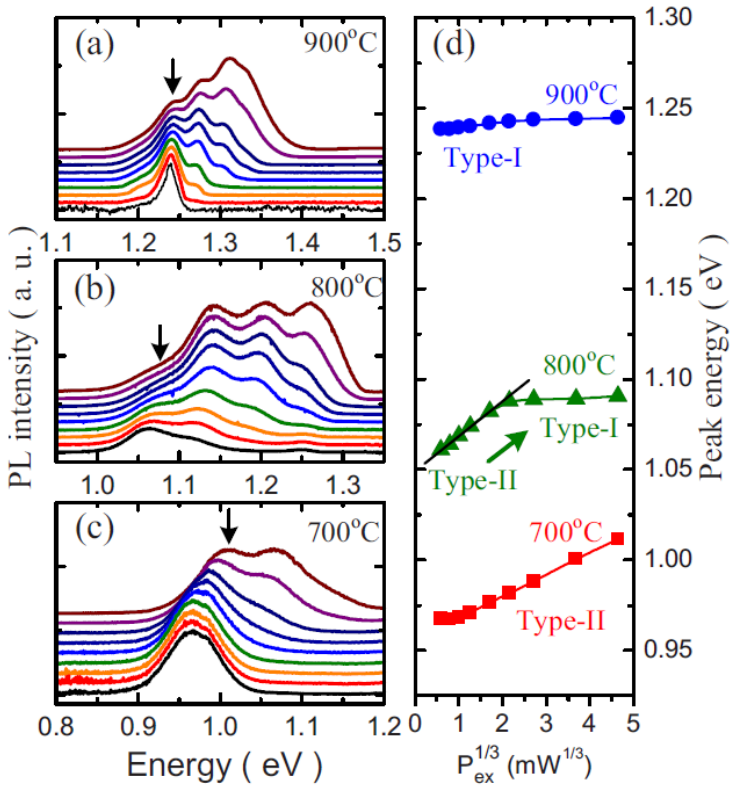

Fig. 2.11: Power dependent PL spectra for the samples annealed at (a) 900 ℃, (b) 800 ℃, and (c) 700 ℃. (d) The peak energy of QD ground state as a function of $P_{ex}^{1/3}$.

In summary, the emission properties of the InAs/GaAs$_{1-x}$Sb$_x$ type-II QDs after thermal annealing have been investigated. Apart from large blueshifts and a pronounced narrowing of the QD emission peak, alloy intermixing also lead to enhanced recombination rates and reduced localized states in the GaAsSb layer. The type-II QD structure has evolved into a type-I alignment after 900 ℃ annealing. We found that it is possible to manipulate between type-I and type-II recombinations in annealed QDs by using different excitation powers. We demonstrated that post growth annealing can be used to tailor the band alignment, the wavefunction overlaps, and hence the recombination dynamics in the InAs/GaAsSb type-II QDs.

2.3. MODULATION OF CAPPING LAYER THICKNESS

Variation of the Sb content in the GaAsSb CL (Sec. 1 in this chapter) and post-growth thermal treatments (Sec. 2 in this chapter) have been employed to tailoring the transition energy, the band alignment, the wave function overlaps and hence the carrier dynamics for specific applications. Another approach is to change the GaAsSb CL thickness, which is expected to affect the quantum confinement of hole states and the strain distribution surrounding the type-II QDs. Furthermore, GaAsSb CL with appropriate thickness is essential for applications with stacked multilayer structure. However, not much attention has been paid to the evolution of optical properties of the GaAsSb-capped InAs/GaAs QDs with the CL thickness.

In this section, we investigate the evolutions of emission energy and recombination lifetime of the GaAsSb-capped InAs/GaAs QDs with the CL thickness. The effects of the CL thickness on the hole states and their wave function distributions are discussed and compared with eight-band **k·p** model calculations.

2.3.1 Experimental details

The samples were grown by MBE. A layer of self-assembled InAs QDs (2.7 MLs) were grown at 500 ℃ on the GaAs buffer layer and subsequently capped by a $GaAs_{0.8}Sb_{0.2}$ layer with a thickness *t*. Four samples with *t*= 0, 2.5, 5 and 10 nm have been grown. The samples were finally capped by a 50 nm GaAs layer. Atomic force microscopy revealed that uncapped surface QDs are lens shaped, with an average height of 8.0 ± 0.5 nm, an average diameter of 20 nm, and an areal density of about 3×10^{10} cm^{-2}.

2.3.2 Effects of GaAsSb capping layer thickness on the optical properties

Figure 2.12 shows the PL spectra measured at T= 12 K for the QD samples under a low excitation power (P_{ex}=10 μW). A clear redshift of the PL peak with the increasing GaAsSb CL thickness is observed. For the nominal Sb content of x = 0.2 in the CL, the InAs-GaAsSb interface is expected to exhibit a type-II band alignment. Therefore the PL redshift with the increasing CL thickness can be attributed to the combined effects of the formation of type-II QDs, the reduced quantum confinement of the hole states, as well as the modifications in the strain distribution in the CL layer. Besides, the $GaAs_{1-x}Sb_x$ capping (with x > 0.2) could increase in the dot height due to the suppressed QD decomposition. However, the evolution of QD size with the GaAsSb CL thickness remains unknown. To gain information about the structural changes by the GaAsSb capping, cross-sectional transmission electron microscopy (TEM) have been performed, which are shown in Fig. 2.13. For the GaAs-capped QDs, the islands are flat in shape, with dimensions of about h= 2.5 nm in height and d= 18 nm in

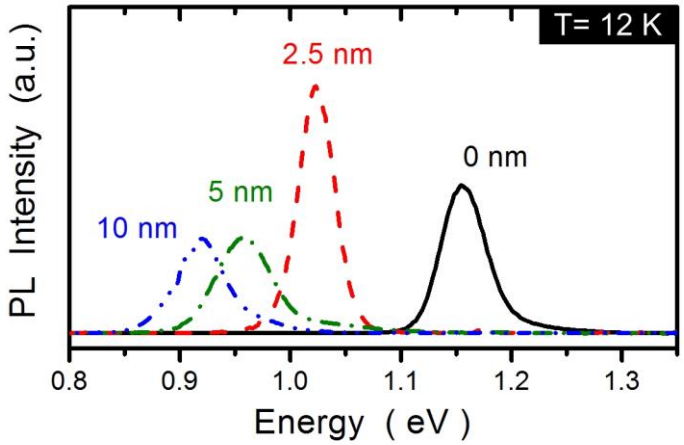

Fig. 2.12: The PL spectra measured at T= 12 K for the investigated QD samples with different CL thickness t.

diameter. After the GaAsSb capping, a gradual increase in the QD size with the CL thickness is observed. The estimated heights (diameters) are 3.1 nm (21 nm), 4.1 nm (21 nm) and 5.2 nm (24 nm) for CL thickness t= 2.5, 5 and 10 nm, respectively. Although accurate determinations of the QD size and shape are hindered by the strong strain field contrast in the TEM images, a clear increasing trend of the QD size with the CL thickness can still be inferred. This means that the enlarged QD size should also be considered in the PL redshift with the CL thickness.

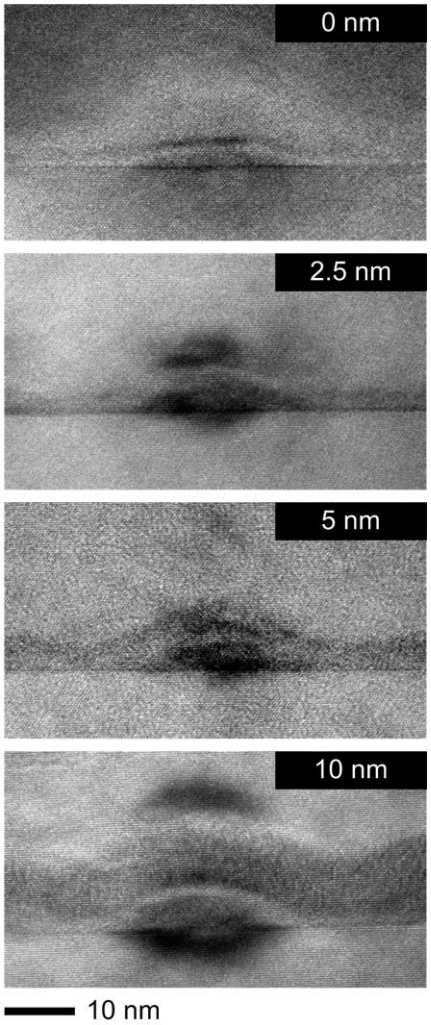

Fig. 2.13: The cross-sectional TEM images for the samples with different CL thicknesses.

To clarify the major effect of the CL thickness, we have performed power dependent PL measurements, which are shown in Fig. 2.14. For the GaAs-capped QDs, the ground-state peak energy remains nearly constant in the investigated power range. By contrast, the GaAsSb-capped samples with t= 5 and 10 nm show large blueshifts with the increasing excitation power, which are clear signatures of the formation of type-II QDs after GaAsSb capping. However, as the CL thickness was reduced to t= 2.5 nm, only a moderate blueshift

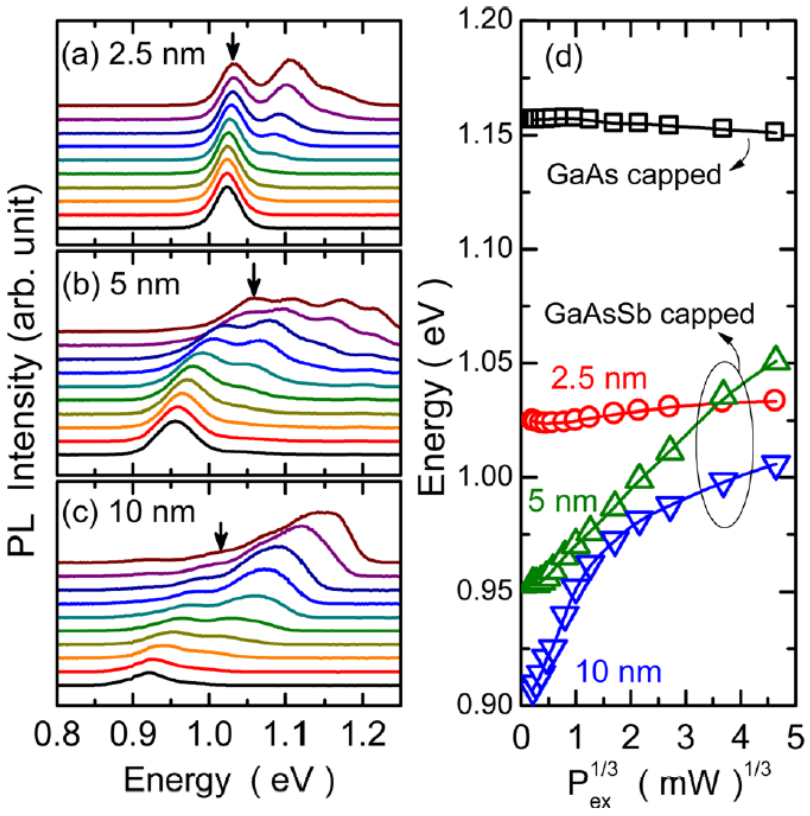

Fig. 2.14: Power-dependent PL spectra for the GaAsSb-capped samples with a CL thickness of (a) 2.5 nm, (b) 5 nm, (c) 10 nm. All the PL spectra have been offset and the intensities have been normalized to their ground-state peak. (d) The ground-state peak energy of the QDs as a function of $P_{ex}^{1/3}$.

of 15 meV is observed. This indicates that a thinner CL thickness tends to reduce the type-II character of the GaAsSb-capped InAs QDs.

The effect of CL thickness on the radiative recombination lifetime in the GaAsSb-capped QDs has also been investigated by TRPL measurements. For a type-II system, the spatially separated electrons and holes would increase the radiative recombination lifetime τ_R, which is inversely proportional to the square of the overlap integral of the electron and hole wave functions and proportional to the emission energy E_{PL} , i.e.,

$$\frac{1}{\tau_R} \propto \frac{|\langle \varphi_e(\mathbf{r}) | \varphi_h(\mathbf{r}) \rangle|^2}{E_{PL}}$$

, where $\varphi_{e(h)}(\mathbf{r})$ is the electron (hole) wave function. Since $\varphi_e(\mathbf{r})$ is still well-confined in the QDs even after the GaAsSb capping, the measured τ_R can thus be a measure of the proportion of $\varphi_h(\mathbf{r})$ that remains in the QDs. Figure 2.15(a) shows the PL decay recorded at

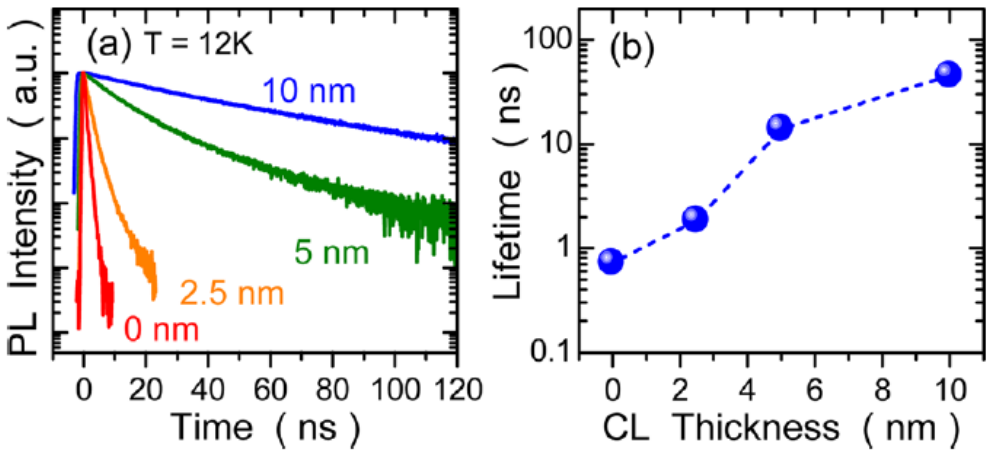

Fig. 2.15: (a) TRPL spectra and (b) the deduced decay time for the investigated QD samples with different CL thickness *t*.

the PL peak under low excitation conditions. The determined τ_R as function of CL thickness are shown in Fig. 2.15(b). For the GaAs-capped InAs QDs, we obtain τ_R= 0.77 ns, which is comparable to the value reported in literature. By contrast, a gradual lengthening of the PL decay time with the increasing CL thickness is observed for the GaAsSb-capped samples. The deduced τ_R are 1.9, 14 and 45 ns for the samples with *t*= 2.5, 5 and 10 nm, respectively. If we assume that $\langle\varphi_e(\mathbf{r})|\varphi_h(\mathbf{r})\rangle = 1$ in the type-I InAs QDs, the overlap in the GaAsSb-capped samples still has 58% for *t*= 2.5 nm, but decreases to 21% and 11% for *t*= 5 and 10 nm, respectively. This means that the hole wave function distribution in the GaAsSb layer is sensitive to the CL thickness, especially for *t* < 5 nm.

2.3.3 Simulations

Theoretical calculations based on eight-band **k·p** model [69] have been performed in order to understand the effects of CL thickness quantitatively. For a comparison purpose, we model the InAs QD as a truncated pyramid with {101} facets and having a conformal $GaAs_{0.8}Sb_{0.2}$ CL covering thereon with a thickness *t*. All the material parameters are adapted from Ref. 70, except that the unstrained valence band offsets and the deformation potentials are obtained from Ref. 71 and 72. The strain-induced piezoelectric polarization has also been included. In order to separate the effects of CL thickness on the hole states and the enlarged QD size on the electron states, we have performed two sets of calculations. In the first set we considered a constant QD size (*h*= 3.5 and *b*= 14 nm) and varying the CL thickness from *t*= 0 to 10 nm. The calculated wave function distributions of the hole ground state on the (110) plane are displayed in Fig. 2.16(a) to (d). For the GaAs-capped QD, the hole is well-confined in the QD with a high wave function overlap up to 98%. With the increasing *t*, the hole wave function penetrates gradually into the GaAsSb layer due to the reduced quantum confinement of hole states in the CL. The hole wave function is localized close to the QD base, in consistent with recent calculations [73]. As *t* is further increased from 5 to 10 nm, the hole

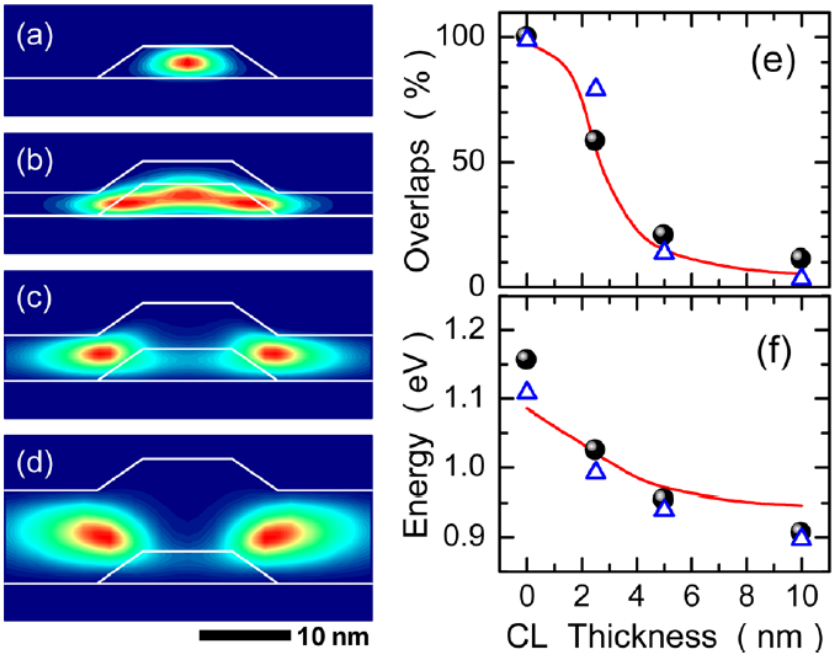

Fig. 2.16: The calculated wave functions of the hole ground state of the InAs QD with a GaAsSb CL thickness of (a) 0 nm, (b) 2.5 nm, (c) 5 nm, and (d) 10 nm. (e) The electron-hole wave function overlaps and (f) the ground state transition energy as a function of the CL thickness, where the solid symbols are experimental data, while the solid curves (open symbols) are calculated results obtained from the first (second) set of calculations.

wave function becomes more extended in the GaAsSb layer. On the other hand, the electron states, as well as their wave function distributions are nearly unchanged by the GaAsSb capping. As shown in Fig. 2.16(e), the calculated wave function overlap (solid curve) decreases gradually from t= 2 to 5 nm and become less dependent on the CL thickness for t > 5 nm, in agreement with the experimental data (solid symbols). In Fig. 2.16(f), the calculated transition energy also shows a redshift with the increasing CL thickness. The overall redshift from t= 0 to 10 nm is 140 meV, which is however smaller than the experimental redshift (~250 meV). In fact, we have also calculated different QD sizes (but keeping a constant size

for all *t*) and found that only minor changes in the overall redshift in the transition energy. This indicates that the different CL thicknesses, which affect predominantly the hole states, cannot fully account for the observed PL redshift. Therefore, in the second set of calculations, we further consider the enlarged QD size induced by the GaAsSb capping according to our TEM analysis. All other parameters are kept the same. As shown in Fig. 2.16(e) and 2.16(f), the experimental energy shift is well reproduced by the second set of calculations (open symbols). This result indicates that the modification in QD size by the GaAsSb capping still plays a nonnegligible role in the evolution of the optical property of the InAs QDs with CL thickness.

We would like to mention that the GaAsSb-capped sample with *t*= 2.5 nm exhibits a stronger PL intensity and a narrower PL linewidth at T= 12 K. This sample also shows a RT PL emission at 1.3 μm with a large enhancement in the integrated intensity (~7×) as compared with the GaAs-capped QDs [see Fig. 2.17]. Such an improvement in the optical properties is very appealing for long-wavelength emitters. Although the increased dot height of the GaAsSb-capped QDs is beneficial for extending the emission wavelength, the

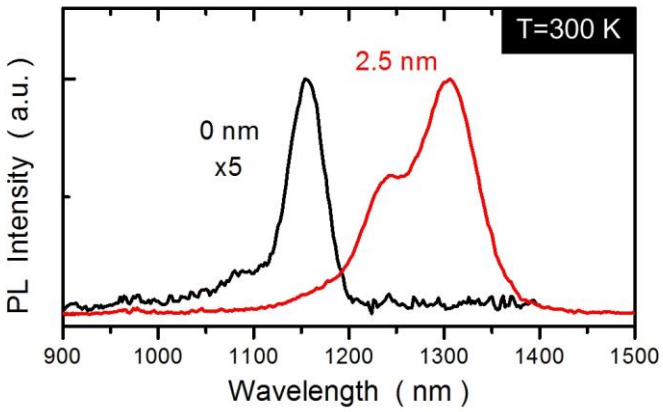

Fig. 2.17: The RT PL spectra for the samples with a CL thickness of *t* = 0 and 2.5 nm.

formation of type-II QDs for higher Sb contents on the other hand hinders them from being efficient light emitters. A trade-off might be researched by optimizing the Sb content in the GaAsSb CL. The study suggests that a careful control of the GaAsSb CL thickness (t < 2.5nm) is an alternative approach for extending the emission wavelength while retaining the type-I characters of the QDs.

In summary, we have used PL and TRPL measurements to study the emission energy and the recombination lifetime of GaAsSb-capped InAs QDs with different CL thicknesses. Theoretical calculations indicated that the PL redshift and the lengthening of PL lifetime arise not only from the modifications in the quantum confinement of hole states in the GaAsSb layer, but also from the Sb induced structural changes in the QDs. Controlling the GaAsSb CL thickness can be an alternative approach for tailoring the optical properties of GaAsSb-capped InAs QDs.

2.4. QUATERNARY ALGAASSB CAPPING LAYER

Longer recombination lifetime makes the type-II InAs/GaAsSb QDs promising for memory and photovoltaic devices, but the degraded recombination efficiency is however detrimental for light emitting devices. Several works have been devoted to the tailoring of the optical properties of GaAsSb-capped InAs QDs. However, since the effects of strain reduction and decomposition suppression are proportional to the Sb content in the CL, it seems unlikely to take the advantages of GaAsSb CL while retaining a type-I QD band alignment. Replacing the GaAsSb by an AlGaAsSb CL appears to be a promising alternative. Figure 2.18(a) shows a contour map of the unstrained VB offset (VBO) between $Al_xGa_{1-x}As_{1-y}Sb_y$ and InAs [i.e., E_V ($Al_xGa_{1-x}As_{1-y}Sb_y$) − E_V (InAs) , where E_V is the valence band maximum] as functions of the Al (x) and the Sb (y) contents according to the material parameters in Ref. 70. If the quaternary AlGaAsSb alloy is used for capping the InAs/GaAs

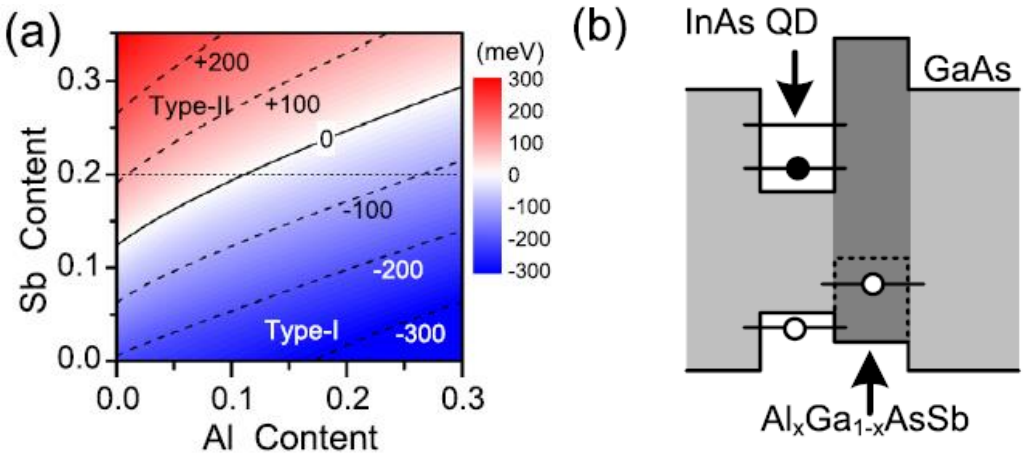

Fig. 2.18: (a) The contour map of the unstrained VBO between $Al_xGa_{1-x}As_{1-y}Sb_y$ and InAs as functions of the Al(x) and the Sb(y) contents. (b) A schematic of band alignments for AlGaAsSb-capped InAs/GaAs QDs.

QDs, the band alignment can be separated into the type-I and type-II regions by the boundary of zero VBO (solid line). Although the boundary line would be changed by the inhomogeneous stain distribution and the quantum confinement of the QDs, it is evident that the band alignment can be restored to type-I by adding Al into the CL when the Sb content exceeds 0.14. Furthermore, InAs/AlGaAsSb QDs can offer stronger electron confinement when the VBO is zero for certain Al and Sb contents in the CL, which is also preferable for the development of QD-based intermediate-band solar cells.

In this section, we demonstrate the tuning of band alignment and optical properties of InAs/GaAs QDs using a thin quaternary AlGaAsSb CL. As evidenced from power dependent PL and TRPL measurements, the GaAsSb-capped QDs with type-II band alignment can be changed to type-I by adding Al into the GaAsSb CL. The evolution of band alignment with the Al content in the CL is also compared with theoretical calculations based on 8-band **k** ·**p** model.

2.4.1 Experimental details

The samples were grown on GaAs substrates by MBE. After the growth of a 200 nm thick GaAs buffer layer on the substrate, a layer of self-assembled InAs QDs (2.7 ML) was deposited at 500 ^{o}C and subsequently capped with a 5 nm thick $Al_xGa_{1-x}As_{1-y}Sb_y$ CL. Four samples with nominal Al contents of x=0, 0.1, 0.2, and 0.3 have been grown. The nominal Sb content is y= 0.2 for all samples. It is worth to mention that the growth rate for the AlGaAsSb layer in all samples was kept the same (500 nm/hr) in order to minimize variations in the Sb incorporation rate and to mitigate Sb segregations. A sample with GaAs capped InAs QDs was also grown as a reference sample of type-I QDs. Finally, all samples were capped by a 50 nm GaAs layer. Atomic force microscopy revealed that uncapped surface QDs are lens shaped, with an average height of 8 nm, an average diameter of 20 nm, and an areal density of about 3×10^{10} cm^{-2}.

2.4.2 The evolution of band alignments

Figure 2.19 shows the PL spectra for the samples measured at T=12 K under a low excitation power of P_{ex}= 10 μW. The QD PL peak blueshifts systematically with increasing Al content x. For the GaAsSb-capped sample (x= 0), the InAs-GaAsSb interface is expected to exhibit a type-II band alignment. Since the lattice constant of $Al_xGa_{1-x}AsSb$ is similar to that of GaAsSb, strain redistribution caused by adding Al into the CL can be excluded. The blueshift in PL peak can thus be attributed to the reduction in the VBO at the InAs-$Al_xGa_{1-x}AsSb$ interface.

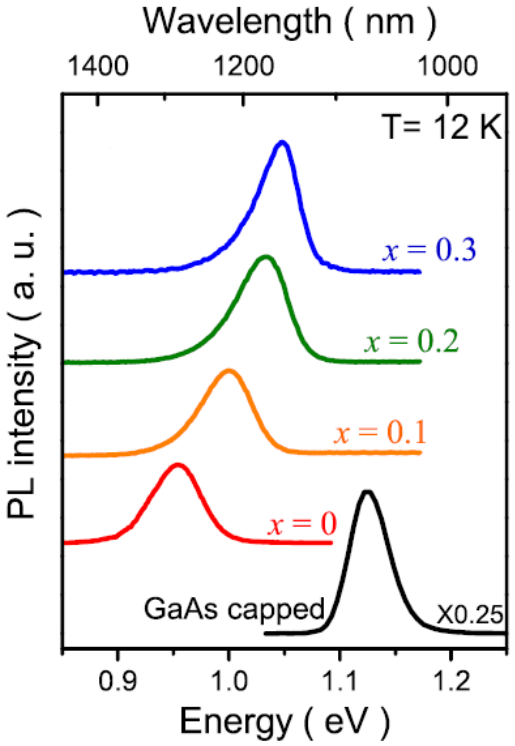

Fig. 2.19: The PL spectra measured at T = 12 K for the GaAs-capped and AlGaAsSb-capped InAs QDs with different Al contents (x).

In order to examine the band alignments, we have performed power dependent PL measurements. Figure 2.20(a) shows the PL peak energy of QD ground state as a function of the cube root of excitation power $P_{ex}^{1/3}$. The PL peak of GaAsSb-capped QDs shows a large energy blueshift with increasing P_{ex} and exhibits a nearly linear dependence on $P_{ex}^{1/3}$, signifying its type-II character. Such an energy blueshift is not observed in the type-I GaAs-capped QDs. For the AlGaAsSb-capped QDs, the PL peak blueshifts at low excitation powers but becomes nearly unchanged under higher excitation conditions. As the Al content x in the CL is increased, the energy blueshift becomes less significant. This behavior can be explained by the gradual evolution from type-II to type-I recombination with the increasing

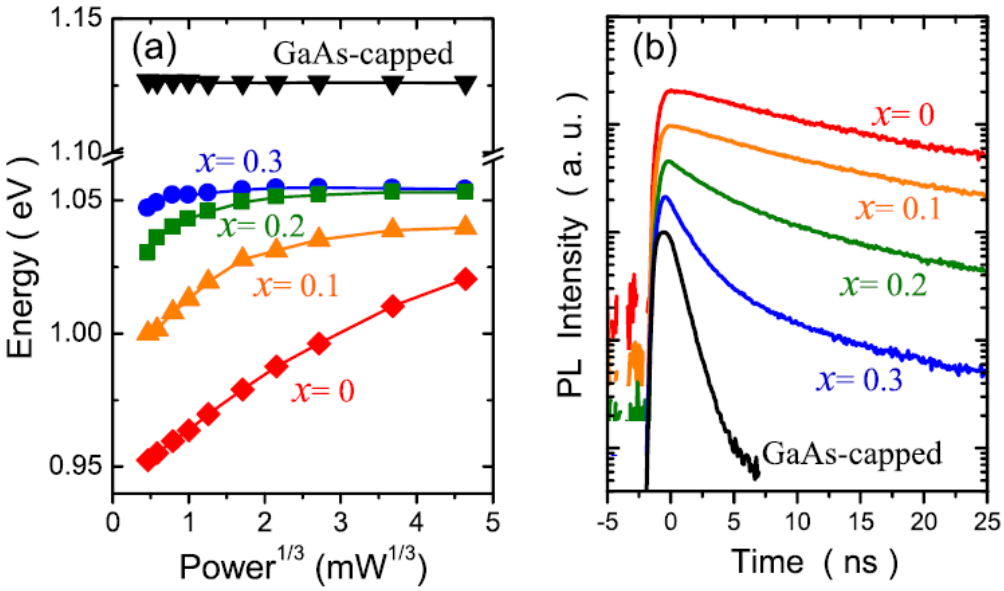

Fig. 2.20: (a) The ground state PL peak energies as a function of $P_{ex}^{1/3}$. (b) TRPL spectra for the investigated samples. (c) The ground state PL peak energies as a function of Al contents (x). (d) The estimated wave function overlaps according to the measured decay lifetimes.

Al content x in the CL. Increasing Al content in the CL tends to reduce the VBO at the QD-CL interface, which becomes unable to confine holes in the CL, resulting in type-I like behaviors. It is remarkable for the AlGaAsSb-capped QDs with x= 0.3, where the PL peak energy is nearly independent of excitation power, indicating that QD-CL interface has changed to a type-I band alignment.

The QD band alignments can be further investigated by TRPL measurements. Figure 2.20(b) shows the TRPL decay traces of the investigated samples measured at T= 12 K. The measured decay lifetime for GaAs-capped QDs in the reference sample is 0.8 ns, comparable to the typical reported value of ~1 ns. In contrast, the GaAsSb-capped sample exhibits a much longer lifetime of 15.7 ns due to its type-II band alignment. Increasing Al content in the CL leads to a significant shortening in decay lifetimes, indicating that more hole wave function penetrate into the QDs. The deduced decay lifetimes are 14.5, 6.5, and 2.2 ns for samples with x= 0.1, 0.2, and 0.3, respectively. Because the radiative recombination lifetime is inversely proportional to the square of the overlap integral of the electron and hole wave functions and proportional to the emission energy, the measured lifetimes can thus be a measure of the electron-hole overlap in the QDs. If we assume that the overlap in the GaAs-capped type-I QDs is 100%, we estimated that the electron-hole overlaps in the $Al_xGa_{1-x}AsSb$-capped QDs are 27, 27, 40, and 70% for samples with x= 0, 0.1, 0.2, and 0.3, respectively.

2.4.3 Simulations

Theoretical calculations based on eight-band **k·p** model [69] have been carried out in order to understand the evolution of hole wave function distribution with the Al content *x* in the CL. We consider the InAs QD as a truncated pyramid with {101} facets and having a base length *b*=14 nm, a height *h*=3.5 nm and a 5 nm $Al_xGa_{1-x}As_{0.8}Sb_{0.2}$ CL covering thereon in a conformal way. The inhomogeneous strain distribution and the strain-induced piezoelectric polarization have also been included. The calculated wave function distributions for the hole ground state on the (110) plane for different Al contents in the CL are depicted in Fig. 2.21(a) to 2.21(d). For the GaAsSb-capped QDs, the hole wave function is localized in the CL and close to the QD base along the [1-10] direction, where the potential is a minimum for the hole. With increasing *x*, the hole wave function penetrates gradually into the QD and eventually well-localized in the QD for $x = 0.3$. This can be attributed to the change of VBO by introducing Al into the CL, as can be seen from the calculated band structures along the growth direction shown in Fig. 2.21(e) to 2.21(h), where the potential minimum for the hole has been moved from the CL to the QD for $x \geq 0.2$. The calculated transition energy and wave function overlaps as function of Al content *x* are displayed in Figs. 2.21(i) and 2.21(j). They fit very well with the measured PL energy shift and the estimated wave function overlaps. For $x < 0.1$, the energy shift rate follows very well with the VBO change rate (4.1 meV/Al%) due to its type-II character. When *x* exceeds 0.2, increasing *x* only leads to higher confined potentials for both the electron and hole, which have less effect on the transition energy of type-I QDs.

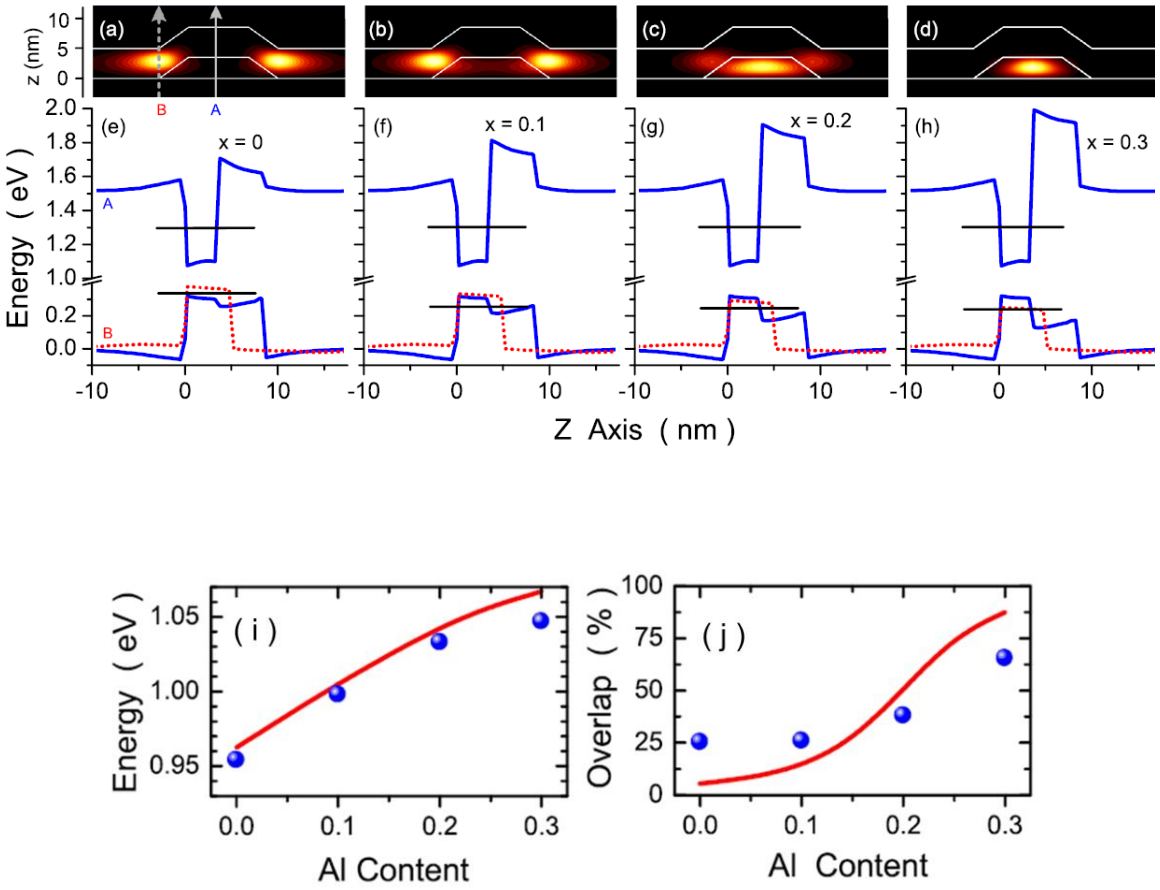

Fig. 2.21: (a)-(d) The calculated wave function distributions for the hole ground state on the (1-10) plane for different Al contents (x=0, 0.1, 0.2, 0.3) in the CL. (e)-(h) The calculated band structures along the growth direction through the center of the QD (solid line, A) and through the CL near the QD base (dotted line, B). (i) The ground state PL peak energies as a function of Al contents and (j) the estimated wave function overlaps according to the measured decay lifetimes, where the curves are the calculated transition energy and wave function overlaps as function of Al content.

We have also performed temperature-dependent PL measurements in order to understand the thermal stability of QD emission property after AlGaAsSb capping. Figure 2.22(a) shows the Arrhenius plot of the integrated PL intensity for GaAs-capped and $Al_{0.3}Ga_{0.7}AsSb$-capped InAs QDs. For the conventional GaAs-capped QDs, the PL intensity started to drop at T > 120 K. In contrast, the PL intensity for the $Al_{0.3}Ga_{0.7}AsSb$-capped sample can persist up to T = 200 K. The thermal activation energy for PL quenching also increases from 371 to 505 meV, implicating the improved thermal stability of QD PL after AlGaAsSb capping. We would like to mention that the $Al_{0.3}Ga_{0.7}AsSb$-capped sample exhibits a large enhancement in the RT PL intensity (×7) as compared with that of the GaAs-capped reference sample [see Fig. 2.22(b)]. Such an improvement in the optical properties makes the AlGaAsSb capped InAs QDs very promising for long wavelength applications.

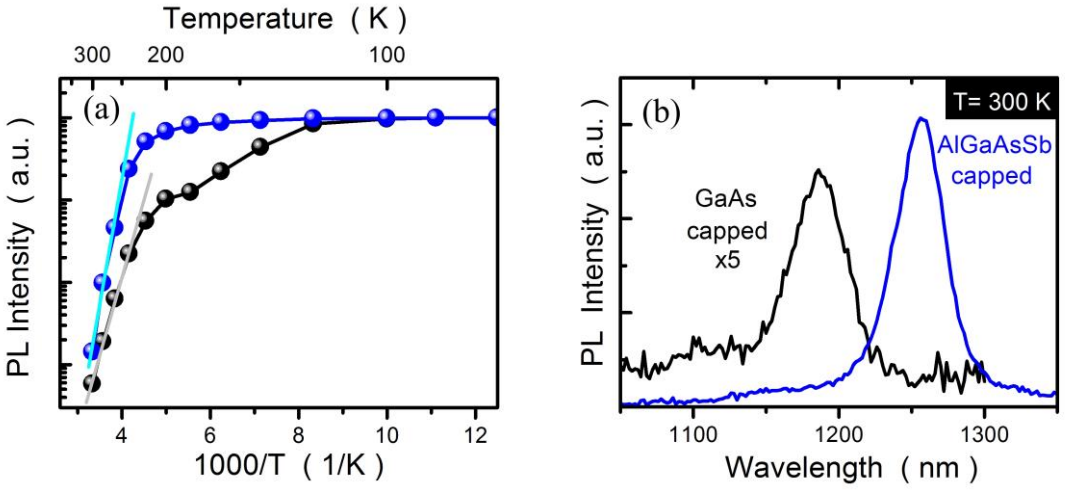

Fig. 2.22: (a) Arrhenius plot of the integrated PL intensity for GaAs-capped and AlGaAsSb-capped InAs QDs with x = 0.3. (b) The PL spectra measured at RT.

In summary, the optical properties of AlGaAsSb-capped InAs QDs have been investigated by PL and TRPL measurements. The original type-II band alignment in GaAsSb-capped InAs QDs can be restored to type-I by adding Al into the CL. Furthermore, the AlGaAsSb CL also improves the PL thermal stability and the RT PL efficiency. We demonstrate that using a quaternary AlGaAsSb CL can take the advantages of GaAsSb CL (i.e., strain reduction and decomposition suppression) on the InAs QDs while retaining their type-I QD characters.

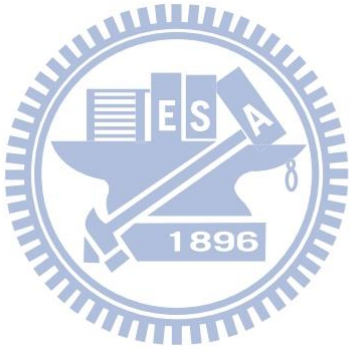

Chapter 3 Device Applications of GaAsSb-Capped InAs Quantum Dots

3.1. QUANTUM-DOT INFRARED PHOTODETECTORS

Self-assembled InAs/GaAs QDIPs have been widely investigated in the past few decades due to its potential advantages of high responsivity, normal incident absorption, and high-temperature operation [74-76]. To manipulate the band structures and the corresponding device performances, changing the CL from GaAs to other materials have been implicated. InGaAs-capped QDIP have achieved the detection wavelength tuning [77,78]. Another possible choice for the CLs over the InAs/GaAs QDs is GaAsSb CLs. The major advantages of the GaAsSb CLs over the InAs QDs include (a) QD strain releasing and (b) the suppression of capping-layer-induced decomposition of the InAs QDs. The two mechanisms would result in PL peak red shift and superior optical characteristics with narrower full-width at half maximum (FWHM) of the PL peaks. It is also observed that by using GaAsSb CLs, improved QD uniformity can be obtained. Therefore, with the superior optical characteristics and QD uniformity of GaAsSb-capped InAs QDs, optimized device performances with narrower spectral responses may be obtained for QDIPs. Although similar device structures have been investigated elsewhere [79], the influence of GaAsSb CL on the device performances and the corresponding transition mechanisms are not fully discussed yet.

In this section, the spectral responses of GaAsSb-capped InAs/GaAs QDIPs with different Sb composition are investigated. The influence of GaAsSb CLs over InAs QDs is also investigated. By comparing the PLE and spectral response curves of standard and

GaAsSb-capped InAs/GaAs QDIPs, different dominant transition mechanisms are observed for these devices. The longer detection wavelengths with narrower spectral widths of GaAsSb-capped QDIPs suggest that this structure can be advantageous for selective detections at specific wavelengths.

3.1.1 Sample structures and device fabrications

The investigated QD samples were grown on (100)-oriented semi-insulating GaAs substrates by Riber compact 21 solid-source MBE system using the SK growth mode. Three samples with ten layers of self-assembled InAs QDs (2.7 MLs) capped by a 5 nm $GaAs_{1-x}Sb_x$ layer with 45 nm GaAs spacer were sandwiched between 300 and 600 nm *n*-GaAs contact layers ($n = 2\times10^{18}$ cm^{-3}) are prepared. The Sb compositions of the three samples are 0, 10 and 20%. The PL measurements are measured by using by a He-Ne laser as the pumping source and an InGaAs photodiode to detect the luminescence. PLE measurements are performed by using Jobin Yvon's NanoLog3 system with a tungsten-halogen lamp as the light source. For the device fabrication, standard photolithography, contact metal evaporation, and wet chemical etching were adopted to fabricate the device with 100×100 μm^2 mesas. The measurement system for spectral response consists of a Perkin-Elmer Spectral 100 Fourier transformation infrared spectrometer, a low-temperature cryostat and a current preamplifier.

3.1.2 Spectral responses and the corresponding transition mechanisms

Figure 3.1(a) shows the PL spectra of the three samples measured at 10 K under a low excitation power of 1 mW. With increasing Sb compositions, a clear red shift in PL peaks is observed with its optimum optical properties, narrowest FWHM and the most intense PL intensity, in *x*=10 % sample. The phenomenon is attributed to the compressive strain relaxation together with the suppressed QD decomposition ability of GaAsSb CLs [40]. In this case, with improved carrier confinement and reduced QD size fluctuation, the PL intensity would increase and PL peak FWHM would decrease for *x*=10 % sample. As for *x*=20 % sample, significant PL intensity declines and broadened FWHM are observed, which

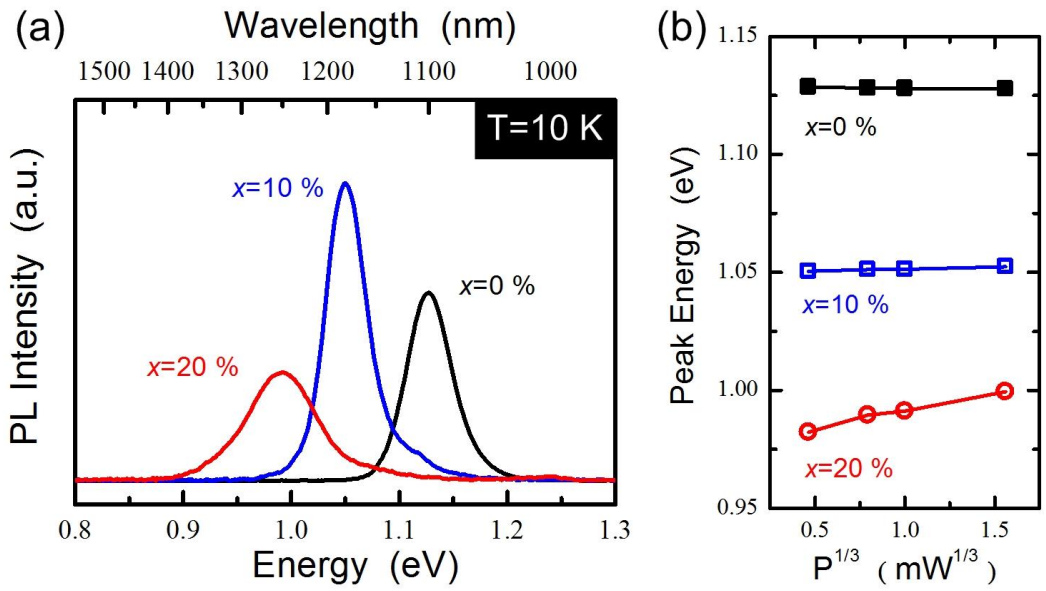

Fig. 3.1: (a) The 10 K PL spectra and (b) PL peaks as a function of cube roots of excitation powers $P^{1/3}$ for GaAsSb-capped samples with different Sb content *x*.

is attributed to the type-I to type-II hetero-interface transition with Sb composition exceeding 14 %. To confirm this attribution, power-dependent PL measurements are performed. As shown in Fig. 3.1(b), energy blue shift of Samples C shows linear dependences on the cube roots of excitation powers $P^{1/3}$, which are consistent with the expected type-II behaviors. On the contrary, the peak positions of x=0 and 10 % sample remain unchanged with increasing pumping powers. Therefore, with increasing Sb compositions in the GaAsSb CLs, the gradually relaxed compressive strain accumulated in the InAs QDs would lead to a band gap shrinkage and PL peak red shift. The FWHM reduction of x=10 % sample is attributed to the improved QD uniformity with the GaAsSb CLs. When Sb composition exceeds 14%, the significant PL intensity decline and FWHM broadenings are attributed to the type-I to type-II hetero-interface transition instead of optical characteristics degradation.

The normalized 10 K spectral responses of the three devices biased at 1.2 V are shown in Fig. 3.2. A significant spectral width reduction of x=10 and 20 % device compared with the x=0 % device is observed. The reference GaAs-capped QDIP (the x=0 % device) exhibits the broadest spectral width $\Delta\lambda/\lambda$ of 0.30 at peak wavelength 6 μm, which is comparable with the typical reported values for such devices. A narrowest $\Delta\lambda/\lambda$ of 0.06 at peak wavelength of 6.78 μm is obtained for the x=20 % device. One possible mechanism responsible for the spectral width narrowing is the improved InAs QD size uniformity. In this case, the narrower spectral widths of GaAsSb-capped InAs QDIPs is consistent with the narrower PL FWHM of the GaAsSb-capped sample with 10 % Sb composition. However, since the improvement in spectral widths is much more significant than that of PL FWHM narrowing, the other mechanism should also be involved for the spectral width narrowing of GaAsSb-capped QDIPs besides the improved QD size uniformity. The other phenomenon observed in the figure is a slight response peak red shift of the x=20 % device compared with the x=10 % device. The result suggests that the energy difference of the confinement states responsible for the intra-band transitions is reduced. For GaAsSb-capped InAs QD structures, larger VB

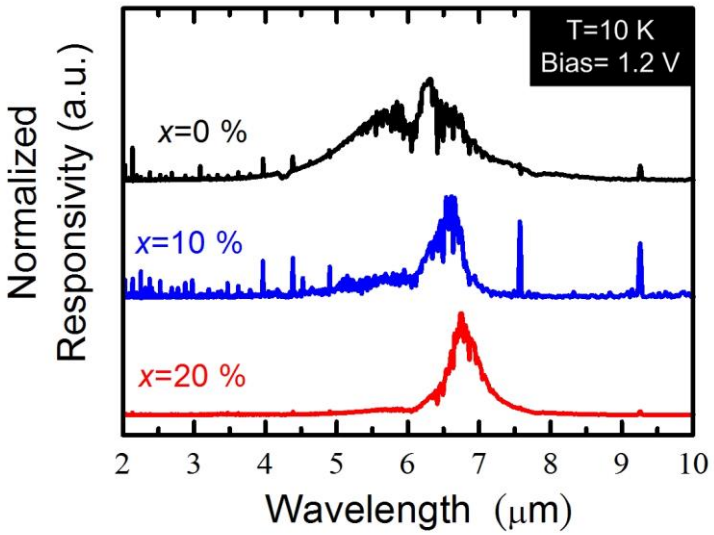

Fig. 3.2: Normalized 10 K spectral responses of GaAsSb-capped devices with different Sb content *x* at 1.2 V.

discontinuity than the conduction band is expected to fall on the interface. In this case, the longer detection wavelengths of GaAsSb-capped QDIPs with higher Sb compositions are directly attributed to the larger InAs QDs resulted from less significant QD decomposition with increasing Sb compositions. The results are different from the response peak blueshift with increasing In compositions of InGaAs-capped QDIPs since there is no additional confinement state appeared with the addition of the GaAsSb CL. Therefore, for InGaAs-capped InAs QDIPs, the possible elongated detection wavelength resulted from InGaAs QW state lowering would be cancelled out by the QD compressive strain relaxation with increasing In composition [80].

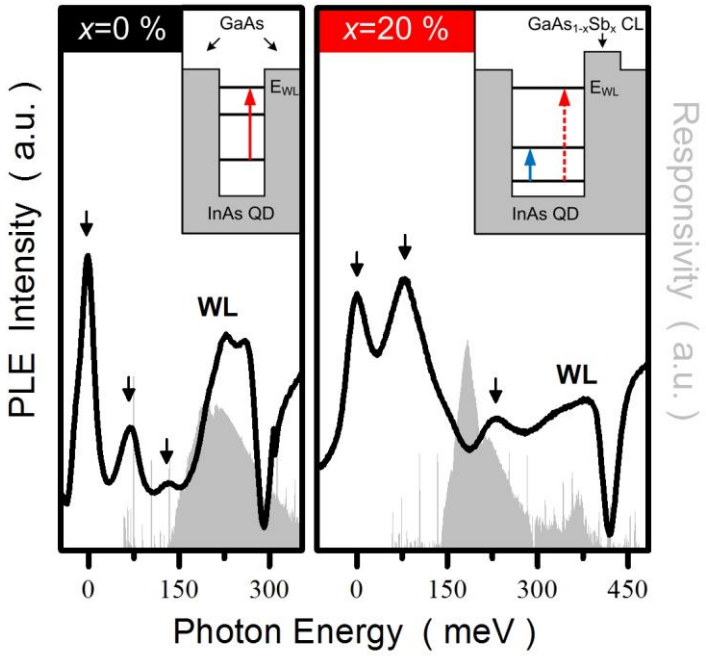

Fig. 3.3: 10 K PLE spectra of x=0 and 20 % sample and 10 K spectral responses of x=0 and 20 % device. The x-axis of the PLE spectra is re-adjusted by setting the QD first excited state as the "zero" energy. The insets depict the schematic conduction band structures and corresponding transitions response for the spectral responses.

To further investigate the transition mechanism of the QDIPs, the PLE measurements are performed on x=0 and 20 % sample. The 10 K PLE spectra of x=0 and 20 % sample with the PL peak energy as the detection energy are shown in Fig. 3.3. By setting the QD first excited state as the "zero" energy, the x-axis of the PLE spectrums are re-adjusted and compared to the spectrum responses of the x=0 and 20 % device operated at 1.2 V, which are also shown in Fig. 3.3. The peaks corresponding to the absorptions of QD bound states and the wetting layer (WL) are noted on the PLE spectrums. As shown in the

figure, for the *x*=0 % device, the spectral response is well agreed with the energy difference ΔE between the QD first excited and WL states. As discussed in previous literatures for traditional InAs QDIPs, the result suggests the broad response comes from the summation of transitions between QD bound and WL states [81,82]. For the *x*=20 % device, a dominant and a weaker response peaks with ΔE=184 meV and ΔE=367 meV are observed on the spectral response curve, respectively. Compared with the PLE spectrum of *x*=20 % sample, the high-energy response should be related to the transition between QD bound states and WL as the case of *x*=0 % device. The low-energy one should attributed to the transitions between QD bound states. The slight miss-alignment between the PLE and spectral response peaks may be resulted from the severe water absorption at ~ 6 μm (207 meV), which may hinder the actual response peaks. The results suggest that the dominant transition mechanism changes from QD excited to WL states to intra-band transition between QD bound states for *x*=0 and 20 % device, respectively. The phenomenon is attributed to the larger InAs QDs resulted from the depression of QD decomposition for GaAsSb-capped InAs QD structures as the case of *x*=20 % device. In this case, along with the influence of strain-relaxation of GaAsSb CLs on InAs, the energy states in the InAs QDs would be lowered and energy difference between the confinement states would decrease. Therefore, for the *x*=20 % device, response peak blue shift corresponding to the QD excited to WL states would be observed, which would result in the dominant transition mechanism change to intra-band transition between QD bound states due to the inverse proportion of absorption coefficient over energy differences.

It has been discussed in the previous publications that larger QDs would lead to lower normal incident absorption for QDIPs [83]. Therefore, to confirm the attribution of larger InAs QDs resulted from depression of QD decomposition with the GaAsSb CLs, the normalized peak responsivity ratios of *x*=0 and 20 % device at 1.2 V under different incident light polarizations are shown in Fig. 3.4. As shown in the figure, although only minor ~ 5 % normal incident absorption ratio difference is observed for the two devices, *x*=20 % device does exhibit lower incident absorption ratio compared with *x*=0 % device. The results are consistent with the previous discussions that by using GaAsSb CLs, QD decomposition will be depressed. In this case, larger InAs QDs are obtained for GaAsSb-capped QDIPs. Therefore, the lowered QD bound states, reduced energy difference in-between the two states and the improved QD uniformity would together contribute to the longer wavelength absorption with narrow spectral widths of GaAsSb-capped QDIPs.

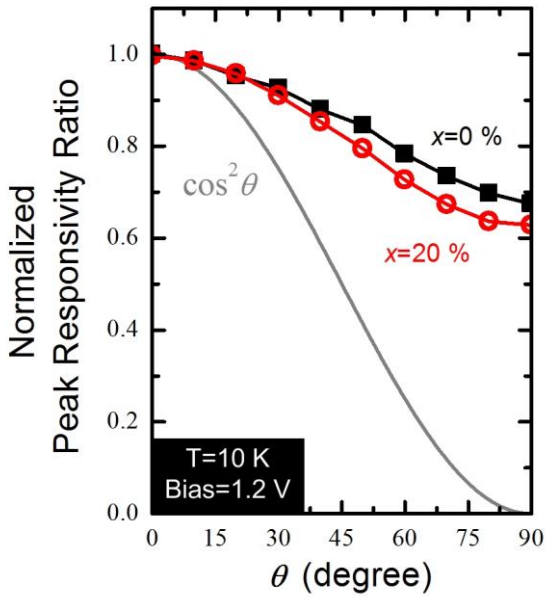

Fig. 3.4: The normalized responsivity ratios of *x*=0 and 20 % device at 1.2 V under different incident light polarizations.

In summary, we investigate the effects of the GaAsSb CLs on the spectral responses of InAs/GaAs QDIPs. An extremely narrow spectral response of $\Delta\lambda/\lambda=0.06$ is observed for the device with 20 % Sb composition. The results suggest that the GaAsSb CLs would depress QD decomposition. In this case, larger InAs QDs with improved QD uniformity is obtained for GaAsSb-capped InAs QD structures, which result in energy level lowering and consequently, reduced energy difference in-between the states. Therefore, compared with standard GaAs-capped QDIPs, GaAsSb-capped QDIPs are of longer detection wavelength and narrower spectral width. The unique characteristic can be advantageous for selective detection at specific wavelengths by using QDIPs.

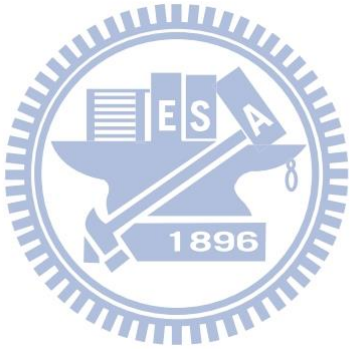

3.2. WIDE-CHANNEL IN-PLANE GATE TRANSISTORS

Besides the applications in optical devices, self-assembled QDs have been proposed as a single element for memory devices. In previous publications, InAs QDs usually acts as a floating gate above a nearby two-dimensional electron gas (2DEG) channel by using a traditional high-electron-mobility transistors (HEMTs) architecture [22-24, 27]. In this case, the charge/discharge of electrons in InAs QDs would influence the drain current of the device under different gate voltage biasing directions. To further simplify the fabrication procedure for practical application, in-plane gate transistors (IPGTs) with micrometer-sized channel widths are adopted and discussed in this section.

Unlike traditional HEMTs with gates above the channels, IPGTs have provided an alternate choice for the fabrications of HEMTs [84-86]. It is generally accepted that nanometer-sized channels are required to avoid high threshold voltages. In this case, nanofabrication techniques such as e-beam lithography are always required for the fabrications of such devices [84-86]. In one of the previous publications, RT transistor behaviors of IPGTs fabricated using repeated atomic-force microscopy (AFM) anode oxidation for electrical isolations are also demonstrated [87,88]. Although the device architecture has greatly simplified the fabrication procedures of HEMTs, the adoption of either e-beam or AFM systems is still disadvantageous for further fabrication procedure simplification. In another publication, IPGTs with micrometer-sized channel widths are fabricated by using standard photolithography [89]. The operation mechanism responsible for the device is the 2DEG depletion resulted from mobile surface electrons manipulated by the external gate voltages. Therefore, if the same mechanism could also be applied to the sheet resistance such as *n*-(InGa)As layers embedded in undoped GaAs, the IPGT architecture can

be easily applied to detectors in the near-infrared range simply by changing the In compositions.

In this section, drain current modulations are observed for an *n*-GaAs sheet resistance embedded in undoped GaAs matrix at RT with channel width of 20 μm. With appropriate doping density of the *n*-GaAs layer, the drain current can be turned off under acceptable negative gate biases. The photocurrent measurements of devices with *n*-GaAs and *n*-$In_{0.1}Ga_{0.9}As$ channels exhibited extended absorption wavelengths for the latter one.

3.2.1 Experimental details and device fabrications

The samples with 50-nm *n*-GaAs layers embedded in undoped GaAs matrix are prepared by RIBER C21 solid-state MBE system. The structure consists of a 30-nm undoped GaAs capping layer, a 50-nm Si-doped GaAs layer, and a 300-nm buffer layer grown on a semi-insulating GaAs substrate. Three samples with doping densities of $n = 1\times10^{18}$, 5×10^{17}, and 1×10^{17} cm^{-3} for the *n*-type GaAs are prepared. The device is fabricated through the standard procedures including photolithography, wet etching, and metal evaporation using a thermal coater. The channel width is 20 μm with 7 μm trenches to separate drain or source and gate terminals. The channel length is 5 μm. The etching depth of the isolating trench is 750 nm, which has penetrated through the *n*-GaAs channels.

3.2.2 Operation mechanisms

The RT I_D–V_{GS} curves of the three devices with different *n*-GaAs doping densities are shown in Fig. 3.5(a). As shown in the figure, because of its highest doping density in the channel, the device with n= 1×10^{18} cm^{-3} cannot be switched off at gate bias −10.0 V. With reduced 5×10^{17} cm^{-3} doping density, the device has revealed standard transistor behaviors in the gate bias ranging from −10 to 5 V. For the device with n= 1×10^{17} cm^{-3}, because of its lowest doping concentration in the *n*-GaAs layer, the lowest saturation drain current is observed. The results suggest that the main mechanism responsible for the current modulation of the devices is the population of surface mobile electrons [89]. The number of mobile surface electrons is highly correlated with the exposed GaAs area to the atmosphere. In this case, if the doping density is too high as the case of the device with n= 1×10^{18} cm^{-3}, the device will not be able to be switched off. On the other hand, the too low doping density

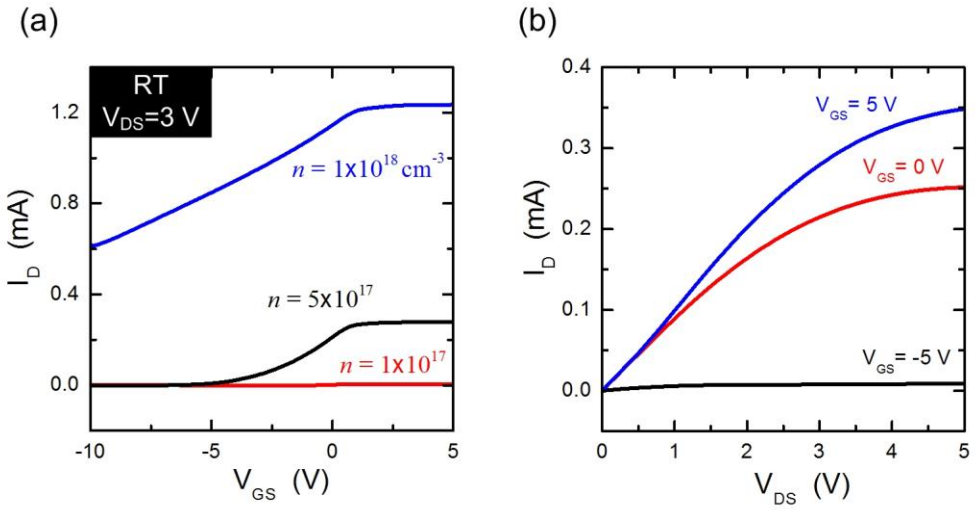

Fig. 3.5: (a) RT I_D–V_{GS} curves of devices with different *n*-GaAs doping density *n*. (b) RT I_D–V_{DS} curves of the device with n= 5×10^{17} cm^{-3} at V_{GS}= 5, 0, and −5 V.

as the case of the device with n= 1×10^{17} cm^{-3} would result in depressed saturation drain currents. Therefore, a trade-off between current modulation and saturation current should be done by optimizing the doping density in the *n*-GaAs channel.

In addition, Fig. 3.5(a) shows the drain current saturation occurred at V_{GS} = 1.2 V for the device with n= 5×10^{17} cm^{-3}, which states that the channel is slightly depleted when no gate bias is applied. In this case, the positive gate bias would attract the surface electrons accumulated on the top of the channels such that the maximum drain current does not occurred at V_{GS} = 0 V. The RT drain current I_D versus drain-source voltage V_{DS} curves of the device with n= 5×10^{17} cm^{-3} at V_{GS} 5, 0, and −5 V are shown in Fig. 3.5(b). As shown in the figure, drain current saturation is observed for the device at higher drain-source voltages. The operation mechanisms of IPGTs are similar to the current flow in a sheet resistance with gate-controllable doping densities. In this case, the phenomenon should be attributed to the drift velocity saturation of semiconductors at high lateral electrical fields [90]. In addition, the figure shows the switch-off behavior of the device at an acceptable V_{GS} of −5 V considering its large channel width 20 μm. The results are consistent with the previous assumption that the channels are not depleted directly by the applied in-plane electric field. The population of mobile electrons is the main mechanism determining the ON–OFF behaviors of IPGTs.

To further explain the operation mechanisms of the devices, the top-view picture and the schematic cross-sectional diagram of the device are shown in Fig. 3.6. Considering the wide channel width and the low gate biases, the limited in-plane electric fields should not be the main mechanism responsible for the drain current modulation. The main mechanism should be the population of mobile surface electrons on the GaAs surface under different gate bias conditions. As shown in the figure, when negative biases are applied to the gate terminals, the mobile surface electrons will be repelled and accumulated on the top of the *n*-GaAs channels. Since the distance between the surface electrons and the channels is only 30 nm, the

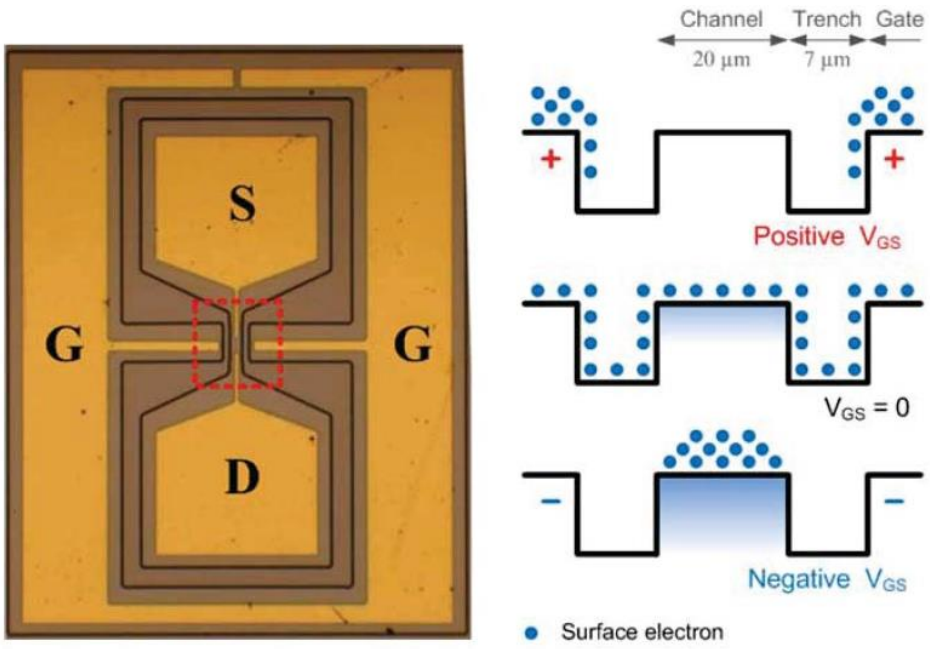

Fig. 3.6: Top-view picture and the schematic cross-sectional diagram of the IPGTs.

accumulated surface electrons could effectively deplete the *n*-GaAs channels. In this case, the drain current would be greatly depressed as the cases of the devices with $n = 5\times10^{17}$ and 1×10^{17} cm^{-3}. At V_{GS}=0 V, the surface electrons should uniformly distribute on the GaAs surfaces. In the case, although part of the electrons in the channels will be depleted, significant drain currents could still be observed given high enough doping densities in the *n*-GaAs layers as the case of the devices with $n = 1\times10^{18}$ and 5×10^{17} cm^{-3}. When positive voltages are applied to the gate terminals, the mobile surface electrons will be attracted to the gate terminals. Hence, higher drain current are observed as the less surface electrons resident in the areas above the channel. This phenomenon is observed in the devices with $n = 1\times10^{18}$ and 5×10^{17} cm^{-3} since the maximum drain currents occur at V_{GS}>0 V.

3.2.3 Photodetector applications

One of the possible applications of the IPGTs is in high-speed phototransistors. The operation speed of the detector is limited by the material mobility instead of the RC time constant of *p*-*n* junctions. With the uncovered channel area to provide large photon absorption region, optimized signal-to-noise ratios may be obtained by applying negative gate biases to depress the dark currents. The detection wavelengths may be extended to the near-infrared range by changing different materials as the channel. To investigate this possibility, another device is prepared by replacing the 50-nm *n*-GaAs channels with 20-nm $In_{0.1}Ga_{0.9}As$ channel *n*-type doped to 1×10^{18} cm^{-3}. The choice of thinner channel thickness is to avoid strain relaxation resulted from lattice mismatched InGaAs layers grown on GaAs substrates. The normalized photocurrents of the device with 20-nm $In_{0.1}Ga_{0.9}As$ channel *n*-type doped to 1×10^{18} $cm^{-3}$and the device with *n*-GaAs channel doped to 5×10^{17} cm^{-3} are shown in Fig. 3.7(a). The measurements conditions are V_{DS}=1 V and V_{GS}=0 V at RT. The photocurrent measurements are done by irradiating the devices with a chopped tungsten-halogen lamp light source by using an optical chopper. A Standard Research Systems SR830 lock-in preamplifier coupled with a SR570 current preamplifier is used to record the corresponding photocurrents of the devices. The drain and gate voltages are supplied by SR570 and the other common-ground power supply. For the device with *n*-GaAs channel doped to 5×10^{17} cm^{-3}, the cutoff absorption wavelength is ~870 nm, which is close to the GaAs band gap at RT. The results demonstrated the potential of the IPGT architecture for photodetector applications. For the device with the *n*-InGaAs channel, except for the photocurrent corresponding to GaAs absorption, additional peak absorption at ~928 nm is observed. Although the results demonstrated the possibility of extended wavelength detection of IPGTs by changing the channel materials, the two separate absorption regions corresponding to GaAs and InGaAs suggest that the photocurrent does not come merely from

the *n*-InGaAs channel.

To further investigate the operation mechanisms of the device with *n*-InGaAs channels, the spectral response curves of the device with a 20-nm *n*-$In_{0.1}Ga_{0.9}As$ channel operated under different gate biases are shown in Fig. 3.7(b). The results are obtained by calibrating the incident powers of the light source with a Thorlabs PM100D power meter. As shown in the figure, the responsivities of the device are one-two orders of magnitudes lower than the conventional InGaAs PIN diodes. A possible reason for this phenomenon is the thin absorption region of the device. Also shown in the figure is that with decreasing gate biases to −9 V, the photocurrent corresponding to the GaAs absorption will gradually disappear. At V_{GS} =−14 V, the photocurrent corresponding to the InGaAs absorption will also disappear.

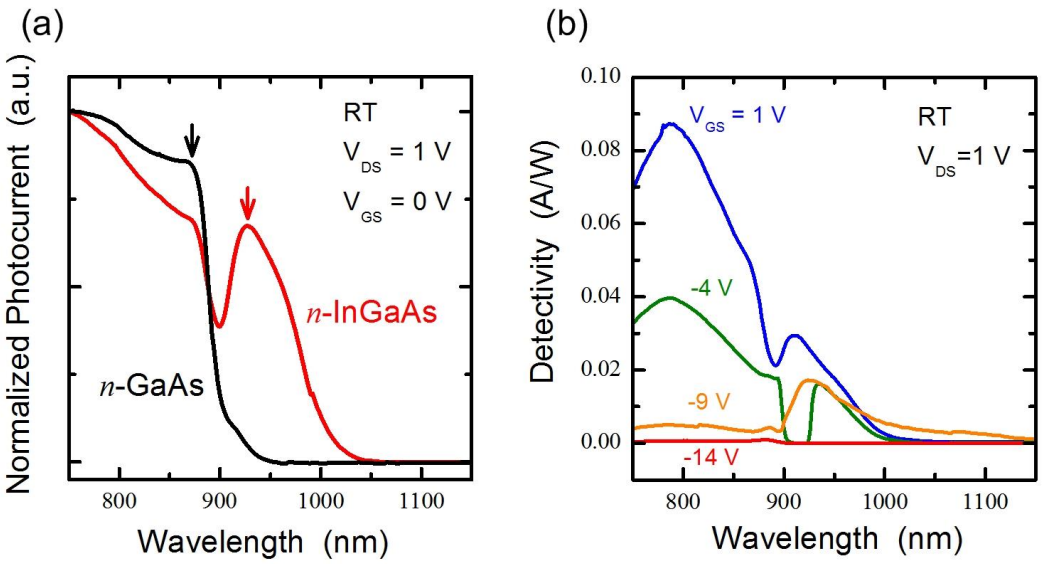

Fig. 3.7: (a) Normalized photocurrents of the device with *n*-GaAs channel doped to 5×10^{17} cm^{-3} and another device with 20-nm $In_{0.1}Ga_{0.9}As$ channel *n*-type doped to 1×10^{18} cm^{-3} operated at V_{DS}=1 V and V_{GS}=0 V at RT. (b) RT spectral response curves of the device with 20-nm $In_{0.1}Ga_{0.9}As$ channel *n*-type doped to 1×10^{18} cm^{-3} operated at V_{DS} = 1 V and different gate biases.

The main device parameter changing with the gate biases is the amount of mobile surface electrons accumulated on the top of the channel. The results suggest that the photo-excited electrons in the top undoped 30-nm GaAs would still contribute to the observed photocurrents of the device. In this case, at V_{GS}=−9 V, although the electric field built by the accumulated surface electrons is still too weak to fully deplete the *n*-InGaAs channel, it is sufficient to deplete the top GaAs layer. With the gate bias further reduced to −14 V, the increasing accumulated surface electrons would build large electric field to deplete *n*-InGaAs channel. The results would be the first disappearance of photocurrents corresponding to GaAs absorption and then the other part to InGaAs absorption with decreasing gate biases. However, since the top GaAs layer is undoped, more detailed investigations should be done to explore how the photo-excited electrons in that layer would flow to the conducting InGaAs layer and contribute to the photocurrent.

In summary, we investigated IPGTs with an *n*-GaAs sheet resistance and 20-μm channel widths. Well current modulation was observed for the sheet resistance with appreciate doping densities in the channel region. The phenomena is due to the channel electron depletion resulted from the population of the mobile surface electrons repelled to the top of the channel with negative gate biases. The photocurrent measurements demonstrated that employing IPGTs with sheet resistance can be an alternative approach for application of high-speed phototransistors.

3.3. MEMORY DEVICES

Lots of efforts have been devoted to the investigations of memory characteristics of InAs/GaAs QDs [21-28]. However, with the type-I nature of InAs/GaAs heterostructures, the fast carrier recombination which relaxes the charge storage radiatively may limit the applications of InAs QDs to memory devices. On the other hand, it has been shown that the band alignment of GaAsSb-capped InAs QDs becomes type-II as the Sb composition exceeds 14 % [40-42], which reduces the unwanted interband carrier recombination. Therefore, by changing the CL from GaAs to GaAsSb, we may further improve the charge-storing capability of InAs QDs. To further simplify the fabrication procedure, IPGTs with micrometer-sized channel widths are adopted in this section to demonstrate the memory effect of GaAsSb-capped InAs QDs. The operation mechanism of the wide-channel IPGTs is the change of 2DEG electron density resulted from the electrical fields built by the different surface electron populations under different gate biases [89]. As discussed in the Sec. 3.2, the same device architecture is also used for the current modulation of a single *n*-type (InGa)As sheet resistance and applied as a photodetector [91]. Therefore, if the same device architecture can also be applied to InAs QD memory devices, the simplified device fabrication procedure would greatly facilitate the feasibility of InAs QDs in memory applications.

3.3.1 Sample structures and experimental setups

The samples investigated in this section are prepared by MBE system. The wafer structures are shown in Fig. 3.8. After the growth of a 15 nm $Al_{0.3}Ga_{0.7}As$ spacer layer on the 300 nm undoped GaAs buffer layer/semi-insulating GaAs substrate, a QD-related region, 20 nm *n*-type $Al_{0.3}Ga_{0.7}As$ barrier (doping concentration 1.2×10^{18} cm^{-3}), and 30 nm *n*-type GaAs layer (1.7×10^{18} cm^{-3}) are grown successively. A thin undoped 2 nm GaAs layer is grown before the QD layer to maintain the same InAs dot morphology for different samples. The QD layer is formed by depositing 2.7 MLs of InAs at 500 ^{o}C and subsequently capped by a 5 nm $GaAs_{1-x}Sb_x$ layer. Two samples with nominal Sb compositions *x* of 0 and 20 % are prepared, which are referred as GaAs-capped and GaAsSb-capped, respectively. For GaAsSb-capped sample, due to a Sb composition exceeding 14 %, the band alignment of InAs/GaAsSb interface is transformed from type-I to type-II. In addition to the two QD

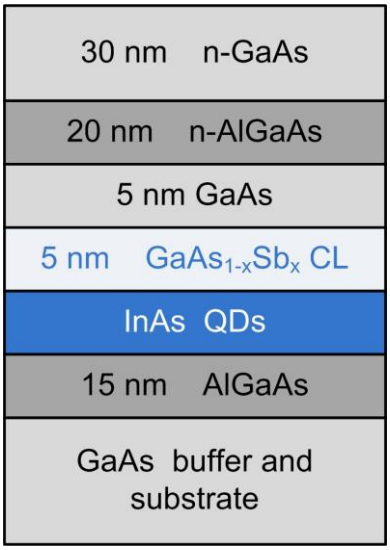

Fig. 3.8: The wafer structures of the investigated QD memory samples.

samples, a reference sample with an identical structure except for the QD-related region, which is replaced with GaAs, is prepared for further comparisons. The IPGTs are then implemented on these samples under the standard procedures including photolithography, wet etching, and metal evaporation using a thermal coater. The channel lengths and widths of these IPGTs are 5 and 20 μm, respectively. Trenches of 7 μm in width are fabricated to separate the drain/source/channel regions from gate terminals. They are 750 nm in depth and penetrate through the 2DEG layers of the three devices. For transient-current measurements, the Keithley 2400 source meter and 6487 picoammeter/voltage source are adopted for the three-terminal device measurement. As the gate-source voltage V_{GS} is varied with the Keithley 2400, the drain currents I_D are recorded using the Keithley 6487 system at a constant drain-source voltage V_{DS} of 1 V. Due to the limit on the time duration between two datum counts of Keithley 6487, the best time resolution of transient-current measurements is about one millisecond. In experiment, the slightly longer time duration of 8.8 ms is adopted to increase the signal-to-noise ratio.

3.3.2 Migration speed of surface mobile electrons

Prior to the investigations of QD charging/discharging behaviors in the IPGTs, an issue to be resolved is whether the surface mobile electrons could follow variations of the gate bias in the millisecond timescale. The RT direct-current (DC) I_D-V_{GS} curve of the reference device is shown in Fig. 3.9(a). From the curve, a standard transistor behavior with clear current modulations as a function of V_{GS} ranging from −10 to 5 V is observed. The transistor behavior of wide-channel IPGTs originates from the mobile charge population induced by the gate bias [89]. In this case, the transport velocity of surface electrons would be the key factor determining whether (1) IPGTs alone introduce non-negligible dilations in time-dependent measurements, and (2) this architecture is suitable for memory devices under fast modulations of the gate bias or not. The RT time-resolved drain currents of the reference

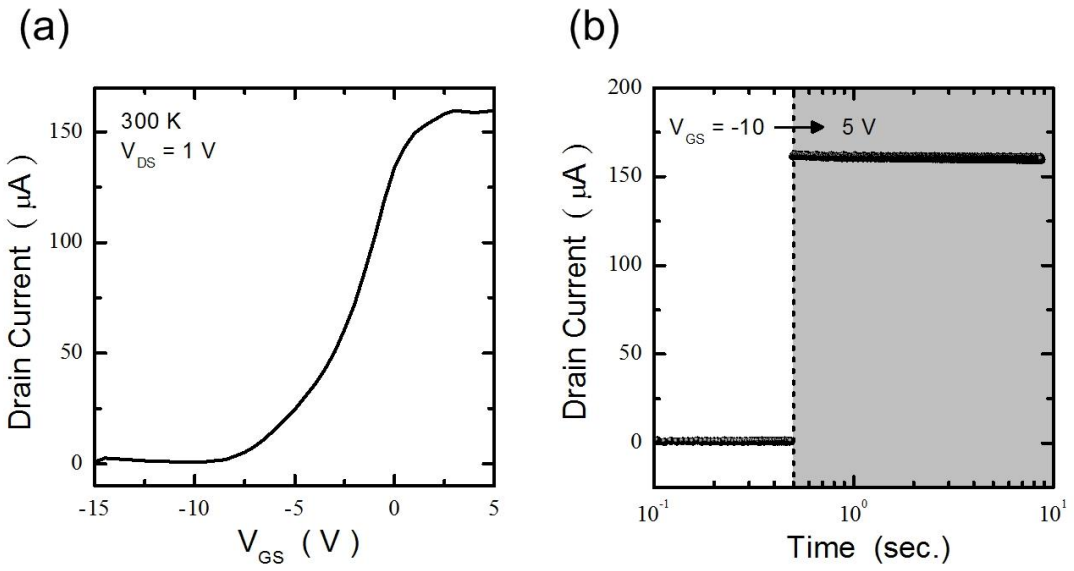

Fig. 3.9: The RT (a) I_D-V_{GS} curve and (b) time-resolved drain currents (V_{GS} jumps from -10 to 5 V at t=0.5 s) of the reference device at V_{DS}=1 V.

device are shown in Fig. 3.9(b). After biasing the reference device in the OFF state at V_{GS} = −10 V, the gate voltage is abruptly changed to ON state (5 V) at a time t=0.5 s. As shown in the figure, the sudden change of the drain current with a delay-free trace in the millisecond range is observed. The result indicates that the response time of surface mobile electrons is at least below the resolution of 8.8 ms. In this way, the issue on the migration speed of surface mobile electrons can be excluded from the following measurements of QD devices. The result also demonstrates the applicability of this architecture in memory devices.

3.3.3 Carrier charging/discharging behaviors

The hysteresis openings of I_D-V_{GS} curves under opposite sweeping directions of the gate bias would take place as the QD layer serves as a floating gate and influences the nearby 2DEG channel [23-28]. The effect has a twofold cause: (1) the carrier density responsible in 2DEG and (2) the QDs filled with electrons may not be identical at the same V_{GS} in the two opposite sweeping processes. The former is responsible for the current conduction while the latter may act as Coulomb scatters and impede the current flow in the nearby 2DEG. If electron exchanges between 2DEG and QDs were fast, such hysteresis phenomena would

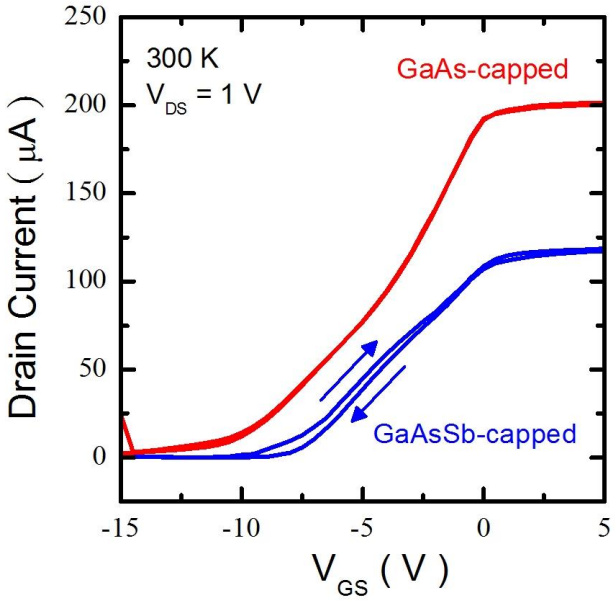

Fig. 3.10: The RT I_D-V_{GS} curves of GaAs-capped and GaAsSb-capped QD devices measured at V_{DS}=1 V under different sweeping directions of the gate bias.

disappear. In the experiment, due to the long electron charging time of QDs, the higher drain current than the ideal one (no hindrance to electron exchanges) would be observed as V_{GS} gradually changes from negative to positive since there are more electrons in 2DEG but fewer ones in QDs than those at equilibrium (QDs slowly get charged). On the other hand, the lower drain current than the equilibrium one should be detected in the opposite sweeping process (QDs gradually turn discharged). The RT I_D-V_{GS} curves of two QD devices at V_{DS} = 1 V under different sweeping directions of the gate bias are shown in Fig. 3.10. The significant clockwise hysteresis is observed in GaAsSb-capped QD device while such a phenomenon is undetected in standard GaAs-capped. The presence of hysteresis openings is the minimum requirement for the usage of these nanostructures to memory devices. The result suggests that applications of type-II InAs/GaAsSb heterostructures to memory devices are more promising than those based on the type-I counterparts.

Although the more significant hysteresis opening of GaAsSb-capped QD device than that of GaAs-capped has indicated the longer electron storage times of type-II GaAsSb-capped InAs QDs than type-I counterparts, the magnitudes of these timescales are still important to practical applications. In Fig. 3.11, we show the RT time-resolved drain currents of two QD devices as V_{GS} jumps from 5 to −5 V at V_{DS} = 1 V. While GaAs-capped QD device exhibits the less prominent but faster current recovery after the sudden reduction, the counterpart of GaAsSb-capped comes to the steady state in the much longer recovery time of about 0.5 sec. For both of the IPGTs in two QD devices, switching V_{GS} from positive to negative results in accumulations of surface mobile electrons above the *n*-type AlGaAs barriers and dispels the electrons in 2DEGs of the corresponding channels. This operation accounts for step-like reductions in the drain currents of the two devices in responses to the bias switching. On the other hand, the distinct recovery times are closely related to the type-I/II nature of the nanostructures.

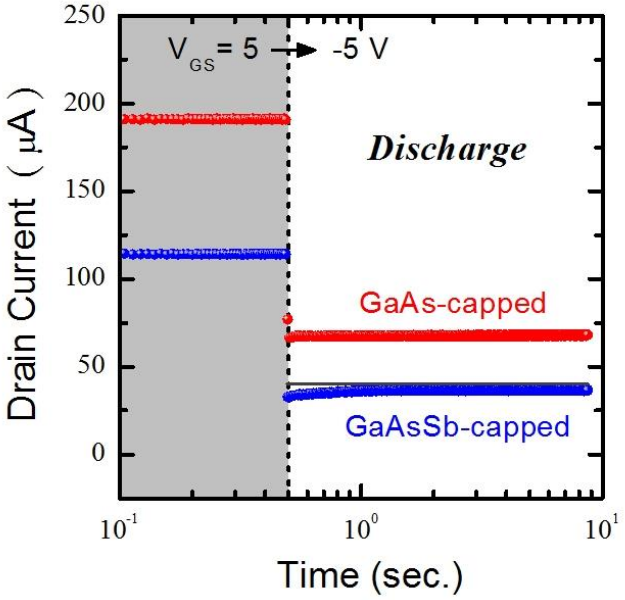

Fig. 3.11: The RT time-resolved drain currents of GaAs-capped and GaAsSb-capped QD devices measured at V_{DS}=1 V. The gate bias V_{GS} changes from 5 to -5 V at t=0.5 s.

In Fig. 3.12(a) and (b), we show the schematic diagrams of GaAs-capped QDs and 2DEG just before and after the switch of V_{GS}, respectively. Since the 2DEG responds to the bias switching (variation of the Fermi level) much faster than QDs do, the originally charged QDs release their excessive electrons at the relatively slower pace. These QDs may discharge through (1) tunneling injections of the electrons to the depleted 2DEG channel, which slightly increases I_D, or (2) interband recombination with the minority holes in bound valence states of QDs. Both processes are not instantaneous and lead to the dilated current response of device A after the bias switching. The discharging process of GaAsSb-capped QDs in device B follows similar scenarios, as indicated in Fig. 3.12(c) and (d). However, the presence of the conduction barrier in the GaAsSb CL further diminishes the wavefunction overlaps between

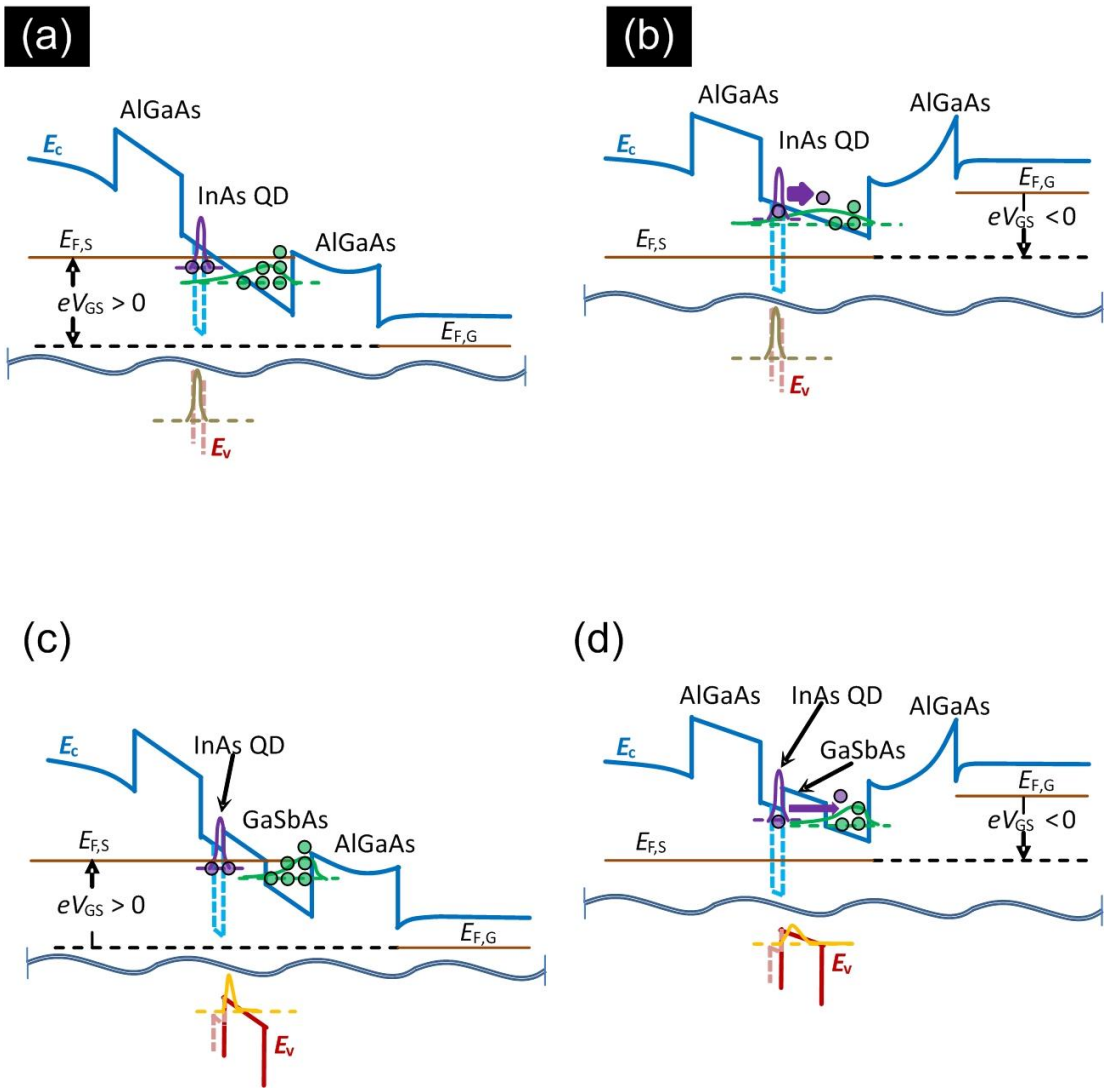

Fig. 3.12: The schematic band diagrams of GaAs-capped QD device (a) before and (b) after the bias switching. The counterparts of GaAsSb-capped are shown in (c) and (d), respectively. The notations $E_{F,G}$ and $E_{F,S}$ represent the Fermi levels near the gate terminal and substrate side, respectively.

QD and channel conduction states and therefore prolongs the tunneling duration. In addition, the type-II nature of the GaSbAs CL eliminates bound valence QD states and turns the interband recombination spatially indirect, which also slowdowns the discharging process. Since both discharging mechanisms are suppressed, the current recovery time becomes significantly longer in GaAsSb-capped QD device than in GaAs-capped.

In addition to the electron discharging phenomena of InAs QDs, it is also important to look into the charging processes in the two devices. The RT time-resolved drain currents of two QD devices as V_{GS} jumps from −15 to 5 V at V_{DS}=1 V are shown in Fig. 3.13. It takes about 1 and 10 s for GaAs-capped and GaAsSb-capped QD devices, respectively, to reach their steady states of current relaxations after the initial current jumps. In this situation, the mobile surface electrons leave the tops of *n*-type AlGaAs barriers in responses to the bias switching, and the 2DEGs in the originally emptied IPGT channels of the two devices are replenished. The electron charging then takes place from the 2DEG to unoccupied conduction states of InAs QDs, which slightly reduces I_D in both devices. The minority holes in QDs or

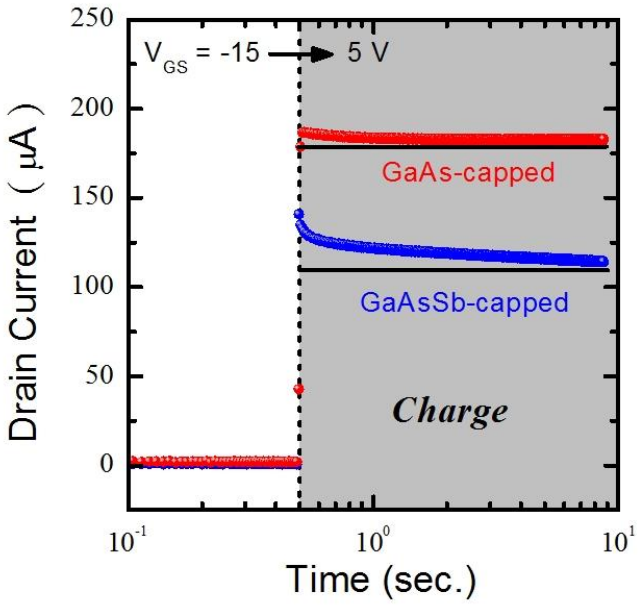

Fig. 3.13: The RT time-resolved drain currents of GaAs-capped and GaAsSb-capped QD devices measured at V_{DS}=1 V. The gate bias V_{GS} changes from -15 to 5 V at t=0.5 s.

the GaSbAs CL may be eliminated by the recombination with electrons in 2DEGs or the injected ones in QDs. Overall, the QD charging can be approximately thought of as the reversed processes of those shown in Fig. 3.12. Still, the GaAsSb-capped QD device exhibits the longer current relaxation time (or QD charging time) than GaAs-capped does due to the GaAsSb CL which plays the roles of conduction barriers and type-II hole separation layers. On the other hand, the charging times of QDs are significantly longer than the discharging counterparts. The further slowdown of the charging processes may have two origins. First, the charging phenomena occur in the bias conditions corresponding to Fig. 3.12(a) and (c). Compared to the discharging processes in Fig. 3.12(b) and (d), the steepened potential due to the positive bias V_{GS} in the charging counterparts further reduces the wavefunction overlaps between the QD and channel conduction states. Hence, the tunneling injections from 2DEGs into QDs become even less efficient than the reversed ones in Fig. 3.12(b) and (d). Second, the charging process increases the local charge density in QDs, which in turn limits the successive injections of electrons into QDs, namely, the effect of Coulomb blockade [92]. These two additional mechanisms further impede carrier exchanges between QD and channel states in charging processes and may lead to the much slower current relaxations in Fig. 3.13 than the corresponding recoveries in Fig. 3.11.

In summary, the charging/discharging behaviors of InAs QDs are demonstrated using the architecture of wider-channel IPGTs at RT. The prompt response of drain currents to the gate bias for the reference device without QDs suggests that the migration speed of surface mobile electrons is sufficiently fast for memory applications. With the GaAsSb capping layer, the InAs QDs have shown the longer electron discharging/charging times than their type-I counterparts. The results have indicated the potential of GaAsSb-capped InAs QDs based on the simple IPGT architecture for memory applications.

Chapter 4 Conclusions

Band structure engineering and device applications of self-assembled InAs QD with a GaAsSb CL have been presented based on our recent investigations. Here we summarize the conclusions as followings.

Four approaches have been adopted to tailor the band alignment of GaAsSb-capped InAs QDs and the corresponding physical features are presented in the first part of this dissertation. First, carrier dynamics of type-II GaAsSb-capped InAs QDs with different Sb composition have been investigated by TRPL measurements. Both the power dependence of PL peak shift and the long decay time constants confirm the type-II band alignment at the GaAsAs-InAs interface. Different recombination paths in such type-II QDs have been clarified by temperature dependent measurements. The long-range recombination with the holes trapped by localized states in the GaAsSb QW is significant at low temperatures. At higher temperatures, the recombination is dominated by the holes confined to the band bending region surrounding the QDs. Second, the emission properties of the InAs/GaAsSb type-II QDs after thermal annealing have been investigated. Apart from large blueshifts and a pronounced narrowing of the QD emission peak, alloy intermixing also lead to enhanced recombination rates and reduced localized states in the GaAsSb layer. The type-II QD structure has evolved into a type-I alignment after 900 ℃ annealing. We found that it is possible to manipulate between type-I and type-II recombinations in annealed QDs by using different excitation powers. The third approach is varying CL thickness of GaAsSb-capped InAs QDs. Theoretical calculations indicated that the PL redshift and the lengthening of PL lifetime arise not only from the modifications in the quantum confinement of hole states in

the GaAsSb layer, but also from the Sb induced structural changes in the QDs. Controlling the GaAsSb CL thickness can be an alternative approach for tailoring the optical properties of GaAsSb-capped InAs QDs. The fourth approach is using the quaternary AlGaAsSb CL. The original type-II band alignment in GaAsSb-capped InAs QDs can be restored to type-I by adding Al into the CL. Furthermore, the AlGaAsSb CL also improves the PL thermal stability and the RT PL efficiency. We demonstrate that using a quaternary AlGaAsSb CL can take the advantages of GaAsSb CL on the InAs QDs while retaining their type-I QD characters. We demonstrate that the four approaches can be used to tailor the band alignment and with great potential for specific applications.

In the second part of this dissertation, two device applications of GaAsSb-capped InAs QDs have been demonstrated. First, we investigate the effects of the GaAsSb CLs on the spectral responses of InAs/GaAs QDIPs. An extremely narrow spectral response of $\Delta\lambda/\lambda=0.06$ is observed for the device with 20% Sb composition. Larger InAs QDs with improved QD uniformity is obtained for GaAsSb-capped InAs QD structures, which result in energy level lowering and consequently, reduced energy difference in-between the states. Therefore, compared with standard GaAs-capped QDIPs, GaAsSb-capped QDIPs are of longer detection wavelength and narrower spectral width. The unique characteristic can be advantageous for selective detection at specific wavelengths by using QDIPs. Second, the architecture of IPGTs is adopted to demonstrate the memory effect of GaAsSb-capped InAs QD. Prior to the investigation of memory device, we studied IPGTs with an *n*-GaAs sheet resistance and 20-μm channel widths. Well current modulation was observed for the sheet resistance with appreciate doping densities in the channel region. The phenomena is due to the channel electron depletion resulted from the population of the mobile surface electrons repelled to the top of the channel with negative gate biases. The photocurrent measurements demonstrated that employing IPGTs with sheet resistance can be an alternative approach for application of high-speed phototransistors. For the charging/discharging behaviors of InAs

QDs using the architecture of wider-channel IPGTs at RT, the prompt response of drain currents to the gate bias for the reference device without QDs suggests that the migration speed of surface mobile electrons is sufficiently fast for memory applications. With the GaAsSb CL, the InAs QDs have shown the longer electron discharging/charging times than their type-I counterparts. The results have indicated the potential of GaAsSb-capped InAs QDs based on the simple IPGT architecture for memory applications.

REFERENCE

1. D. Bimberg, M. Grundmann, and N. N. Ledentsov, *Quantum Dot Heterostructures* (Wiley, Chichester, 1999).
2. M. Sugawara, *Self-Assembled InGaAs/GaAs Quantum Dots*, Vol. 60 of Semiconductor and Semimetals, edited by R. K. Willardson and E. R. Weber (Academic Press, New York, 1999).
3. I. N. Stranski and L. Krastanow, Sitzungsberichte d. Akad. D. Wissenschaften in Wien, Abt. Iib, Band **146**, p. 797 (1937).
4. D. J. Eaglesham and M. Cerullo, Phys. Rev. Lett. **64**, 1943 (1990).
5. F. C. Frank and J. H. van der Merwe, Proc. Roy. Soc. Lond. A **198**, 205 (1949).
6. M. Volmer and A. Weber, Z. Phys. Chem. **119**, 277 (1926).
7. C. W. Synder, B. G. Orr, D. Kessler, and L. M. Sander, Phys. Rev. Lett. **66**, 3032 (1991).
8. D. Leonard, M. Krishnamurthy, C. M. Reaves, S. P. DenBaars, and P. M. Petroff, Appl. Phys. Lett. **63**, 3203 (1993).
9. A. Madhukar, Q. Xie, P. Chen, and Konkar, Appl. Phys. Lett. **64**, 2727 (1994).
10. J. M. Moison, F. Houzay, F. Barthe, Leprince, E. Andre, and O.Vatel, Appl. Phys. Lett. **64**, 196 (1994).
11. D. Bimberg, QUEST Workshop on Quantum Structures, Colloquium Abstracts, Santa Barbara, p. 15.
12. Y. Arakawa, and H. Sakaki, Appl. Phys. Lett. **40**,939 (1982).
13. N. Kirstaedter, N. N. Ledentsov, M. Grundmann, D. Bimberg, V. M. Ustinov, S. S. Ruvimov, M.V. Maximov, P. S. Kop'ev, Zh. I. Alferov, U. Richter, P. Werner, U. Gösele, and J. Heydenreich, Electron. Lett. **30**, 1416 (1994).
14. N. Kirstaedter, O.G. Schmidt, N. N. Ledentsov, D. Bimberg, V. M. Ustinov, A. Yu. Egorov, A. E. Zhukov, M. V. Maximov, P. S. Kop'ev and Zh. I. Alferov, Appl. Phys. Lett.

69, 1226 (1996).

15. D. Bimberg, N. N. Ledentsov, M. Grundmann, N. Kirstaedter, O.G. Schmidt, M.-H. Mao, V. M. Ustinov, A. Yu. Egorov, A. E. Zhukov, P. S. Kop'ev, Zh. I. Alferov, S. S. Ruvimov, U. Gösele, and J. Heydenreich, Jpn. J. Appl. Phys. **35**, 1311 (1996).
16. M. V. Maximov, Yu. M. Shernyakov, A. F. Tsatsul'nikov, A. V. Lunev, A. V. Sakharov, V. M. Ustinov, A. Yu. Egorov, A. E. Zhukov, A. R. Kovsh, P. S. Kop'ev, L. V. Asryan, Zh. I. Alferov, N. N. Ledentsov, D. Bimberg, A. O. Kosogov, and P. Werner, J. Appl. Phys. **83**, 5561 (1998).
17. N. N. Ledentsov, V. A. Shchukin, M. Grundmann, N. Kirstaedter, J. Böhrer, O. G. Schmidt, D. Bimberg, V. M. Ustinov, A. Yu. Egorov, A. E. Zhukov, P. S. Kop'ev, S. V. Zaitsev, N. Yu. Gordeev, Zh. I. Alferov, A. I. Borovkov, A. O. Kosogov, S. S. Ruvimov, P. Werner, U. Gosele, and J. Heydenreich, Phys. Rev. B **54**, 8743 (1996).
18. S. L. Chung and N. holonyak, Appl. Phys. Lett. **80**, 1270 (2002).
19. A. Marent, M. Geller, A. Schliwa, D. Feise, K. Pötschke, D. Bimberg, N. Akçay, and N. Ö ncan, Appl. Phys. Lett. **91**, 242109 (2007).
20. M. Geller, A. Marent, T. Nowozin, D. Bimberg, N. Akçay, and N. Ö ncan, Appl. Phys. Lett. **92**, 092108 (2008).
21. J. J. Finley, M. Skalitz, M. Arzberger, A. Zrenner, G. Böhm, and G. Abstreiter, Appl. Phys. Lett. **73**, 2618 (1998).
22. K. Koike, K. Saitoh, S. Li, S. Sasa, M. Inoue, and M. Yano, Appl. Phys. Lett. **76**, 1464 (2000).
23. C. Balocco, A. M. Song, and M. Missous, Appl. Phys. Lett. **85**, 5911 (2004).
24. D. Nataraj, N. Ooike, J. Motohisa, and T. Fukui, Appl. Phys. Lett. **87**, 193103 (2005).
25. C. R. Müller, L. Worschech, J. Heinrich, S. Höfling, and A. Forchel, Appl. Phys. Lett. **93**, 063502 (2008).
26. E. S. Kannan, G.-H. Kim, and D. A. Ritchie, Appl. Phys. Lett. **95**, 143506 (2009).
27. B. Marquardt, M. Geller, A. Lorke, D. Reuter, and A. D. Wieck, Appl. Phys. Lett. **95**, 022113 (2009).
28. T. Nowozin, A. Marent, G. Hönig, A. Schliwa, D. Bimberg, A. Beckel, B. Marquardt, A. Lorke, and M. Geller, Phys. Rev. B **84**, 075309 (2011).
29. A. Luque and A. Marti, Phys. Rev. Lett. **78**, 5014 (1997).

30. A. Luque, A. Marti, N. Lopez, E. Antolin, E. Canovas, C. Stanley, C. Farmer, L. J. Caballero, L. Cuadra and J. L. Balenzategui, Appl. Phys. Lett. **87**, 083505 (2005).

31. R. B. Laghumavarapu, A. Moscho, A. Khoshakhlagh, M. El-Emawy, L. F. Lester and D. L. Huffaker, Appl. Phys. Lett. **90**, 173125 (2007).

32. S. M. Hubbard, C. D. Cress, C. G. Bailey, R. P. Raffaelle, S. G. Bailey and D. M. Wilt, Appl. Phys. Lett. **92**, 123512 (2008).

33. R. B. Laghumavarapu, M. El-Emawy, N. Nuntawong, A. Moscho, L. F. Lester and D. L. Huffaker, Appl. Phys. Lett. **91**, 243115 (2007).

34. J. M. Ripalda, D. Granados, Y. González, A. M. Sánchez, S. I. Molina, and J. M. García, Appl. Phys. Lett. **87**, 202108 (2005).

35. H. Y. Liu, M. J. Steer, T. J. Badcock, D. J. Mowbray, M. S. Skolnick, P. Navaretti, K. M. Groom, M. Hopkinson, and R. A. Hogg, Appl. Phys. Lett. **86**, 143108 (2005).

36. K. Nishikawa, Y. Takeda, K. Yamanaka, T. Motohiro, D. Sato, J. Ota, N. Miyashita, and Y. Okada, J. Appl. Phys. **111**, 044325 (2012).

37. D. Sato, J. Ota, K. Nishikawa, Y. Takeda, N. Miyashita, and Y. Oada, J. Appl. Phys. **112**, 094305 (2012).

38. K. Nishi, H. Saito, S. Sugou, and J.-S Lee, Appl. Phys. Lett. **74**, 1111 (1999); V. M. Ustinov, N. A. Maleev, A. E. Zhukov, A. Yu. Egorov, A. V. Lunev, B. V. Volovik, I. L. Krestnikov, Yu. G. Musikhin, N. A. Bert, P. S. Kop'ev, Zh. I. Alferov, N. N. Ledentsov, and D. Bimberg, *ibid.* **74**, 2815 (1999); N.-T. Yeh, T.-E. Nee, J.-I. Chyi, T. M. Hsu, and C. C. Huang, *ibid.* **76**, 1567 (2000); W.-H. Chang, H.-Y. Chen, H.-S Chang, W.-Y Chen, T. M. Hsu, T.-P. Hsieh, J.-I Chyi, and N.-T. Yeh, *ibid.* **86**, 131917 (2005); P.-C. Chiu, W.-S. Liu, M.-J. Shiau, J.-I. Chyi, W.-Y. Chen, H.-S. Chang, and T.-M. Hsu, *ibid.* **91**, 153106 (2007).

39. J. M. Ulloa, I. W. D. Drouzas, P. M. Koenraad, D. J. Mowbray, M. J. Steer, H. Y. Liu, and M. Hopkinson, Appl. Phys. Lett. **90**, 213105 (2007).

40. J. M. Ulloa, R. Gargallo-Caballero, M. Bozkurt, M. del Moral, A. Guzmán, P. M. Koenraad, and A. Hierro, Phys. Rev. B **81**, 165305 (2010).

41. H. Y. Liu, M. J. Steer, T. J. Badcock, D. J. Mowbray, M. S. Skolnick, F. Suarez, J. S. Ng, M. Hopkinson, and J. P. R. David, J. Appl. Phys. **99**, 046104 (2006).

42. C. Y. Jin, H. Y. Liu, S. Y. Zhang, Q. Jiang, S. L. Liew, M. Hopkinson, T. J. Badcock, E. Nabavi, and D. J. Mowbray, Appl. Phys. Lett. **92**, 021102 (2007).

43. Y. D. Jang, T. J. Badcock, D. J. Mowbray, M. S. Skolnick, J. Park, D. Lee, H. Y. Liu, M. J. Steer, and M. Hopkinson, Appl. Phys. Lett. **92**, 251905 (2008).

44. W.-H. Chang, Y.-A. Liao, W.-T. Hsu, M.-C. Lee, P.-C. Chiu, and J.-I. Chyi, Appl. Phys. Lett. **93**, 033107 (2008).

45. W.-S. Liu, H.-M. Wu, F.-H. Tsao, T.-L. Hsu, J.-I. Chyi, Solar Energy Material & Solar Cells **105**, 237 (2012).

46. M. Y. Levy and C. Honsberg, IEEE Trans. Electron Device **55**, 706 (2008).

47. Y.-A. Liao, W.-T. Hsu, P.-C. Chiu, J.-I. Chyi, and W.-H. Chang, Appl. Phys. Lett. **94**, 053101 (2009).

48. J. M. Ulloa, J. M. Llorens, B. Alén, D. F. Reyes, D. L. Sales, D. González, and A. Hierro, Appl. Phys. Lett. **101**, 253112 (2012).

49. W.-T. Hsu, Y.-A. Liao, F.-C. Hsu, P.-C. Chiu, J.-I. Chyi, and W.-H. Chang, Appl. Phys. Lett. **99**, 073108 (2011).

50. A. Hospodková, , M. Zíková, J. Pangrác, J. Oswald, K. Kuldová, J. Vyskočil, and E. Hulicius, J. Cryst. Growth **370**, 303 (2013).

51. J. M. Ulloa, D. F. Reyes, M. Montes, K. Yamamoto, D. L. Sales, D. Gonzalez, A. Guzman, and A. Hierro, Appl. Phys. Lett. **100**, 013107 (2012).

52. W.-S Liu, D. M.-T. Kuo, J.-I. Chyi, W.-Y. Chen, H.-S. Chang, and T.-M. Hsu, Appl. Phys. Lett. **89**, 243103 (2006).

53. Y.-A. Liao, W.-T. Hsu, S.-H. Huang, P.-C. Chiu, J.-I. Chyi, and W.-H. Chang, Appl. Phys. Lett. **102**, 173104 (2013).

54. N. N. Ledentsov, J. Böhrer, M. Beer, F. Heinrichsdorff, M. Grundmann, D. Bimberg, S. V. Ivanov, B. Ya. Meltser, S. V. Shaposhnikov, I. N. Yassievich, N. N. Faleev, P. S. Kop'ev, and Zh. I. Alferov, Phys. Rev. B **52**, 14058 (1995).

55. R. Heitz, M. Veit, N. N. Ledentsov, A. Hoffmann, D. Bimberg, V. M. Ustinov, P. S. Kop'ev, and Zh. I. Alferov, Phys. Rev. B **56**, 10435 (1997).

56. U. E. H. Laheld, F. B. Pedersen, and P. C. Hemmer, Phys. Rev. B **52**, 2697 (1995).

57. C.-K. Sun, G. Wang, J. E. Bowers, B. Brar, H.-R. Blank, H. Kroemer, and M. H. Pilkuhn, Appl. Phys. Lett. **68**, 1543 (1996).

58. F. Hatami, M. Grundmann, N. N. Ledentsov, F. Heinrichsdorff, R. Heitz, J. Böhrer, D. Bimberg, S. S. Ruvimov, P. Werner, V. M. Ustinov, P. S. Kop'ev, and Zh. I. Alferov,

Phys. Rev. B **57**, 4635 (1998).

59. Y.-H. Cho, G. H. Gainer, A. J. Fischer, J. J. Song, S. Keller, U. K. Mishra, and S. P. DenBaars, Appl. Phys. Lett. **73**, 1370 (1998).

60. L. Grenouillet, C. Bru-Chevallier, G. Guillot, P. Gilet, P. Duvaut, C. Vannuffel, A. Million, and A. Chenevas-Paule, Appl. Phys. Lett. **76**, 2241 (2000).

61. P. G. Eliseev, P. Perlin, J. Lee, and M. Osiński, Appl. Phys. Lett. **71**, 569 (1997).

62. R. Leon, Y. Kim, C. Jagadish, M. Gal, J. Zou, and D. J. H. Cockayne, Appl. Phys. Lett. **69**, 1888 (1996).

63. S. Malik, C. Roberts, R. Murray, and M. Pate, Appl. Phys. Lett. **71**, 1987 (1997).

64. S. J. Xu, X. C. Wang, S. J. Chua, C. H. Wang, W. J. Fan, J. Jiang, and X. G. Xie, Appl. Phys. Lett. **72**, 3335 (1998).

65. R. Leon, S. Fafard, P. G. Piva, S. Ruvimov, and Z. Liliental-Weber, Phys. Rev. B **58**, R4262 (1998).

66. S. Fafard and C. Nì. Allen, Appl. Phys. Lett. **75**, 2374 (1999).

67. T. M. Hsu, Y. S. Lan, W.-H. Chang, N. T. Yeh, and J.-I. Chyi, Appl. Phys. Lett. **76**, 691 (2000).

68. S. F. Chichibu, T. Onuma, T. Sota, S. P. DenBaars, S. Nakamura, T. Kitamura, Y. Ishida, and H. Okumura, J. Appl. Phys. **93**, 2051 (2003).

69. Numerical calculations were performed using the nextnano^3 3D nanodevice simulators

70. I. Vurgaftman, J. R. Meyer, and L. R. Ram-Mohan, J. Appl. Phys. **89**, 5815 (2001).

71. S.-H. Wei and A. Zunger, Appl. Phys. Lett. **72**, 2011 (1998).

72. S.-H. Wei and A. Zunger, Phys. Rev. B **60**, 5404 (1999).

73. P. Klenovsky´, V. Kr˘a´pek, D. Munzar, and J. Humlı´c˘ek, Appl. Phys. Lett. **97**, 203107 (2010).

74. P. Bhattacharya, X.-H. Su, S. Chakrabarti, G. Ariyawansa, and A. G. U. Perera, Appl. Phys. Lett. **86,** 191106 (2005).

75. Z. Chen, E. T. Kim, and A. Madhukar, Appl. Phys. Lett. **80,** 2490 (2002).

76. S.-Y. Lin, Y.-R. Tsai, and S.-C. Lee, Appl. Phys. Lett. **78,** 2784 (2001).

77. W.-H. Lin, C.-C. Tseng, K.-P. Chao, S.-C. Mai, S.-Y. Lin, and M.-C. Wu, IEEE Photon.

Technol. Lett. **22,** 227 (2010).

78. S.-Y. Lin, W.-H. Lin, C.-C. Tseng, K.-P. Chao, and S.-C. Mai, Appl. Phys. Lett. **95**, 123504 (2009).

79. C.-T. Huang, Y.-C. Chen, and S.-C. Lee, Appl. Phys. Lett. **100,** 043512 (2012).

80. W.-H. Lin, K.-P. Chao, C.-C. Tseng, S.-C. Mai, S.-Y. Lin and M.-C. Wu, J. Appl. Phys. **106**, 054512 (2009).

81. H. C. Liu, M. Gao, J. McCaffrey, Z. R. Wasilewski, and S. Fafard, Appl. Phys. Lett. **78**, 79 (2001).

82. C.-C. Tseng, S.-T. Chou, S.-Y. Lin, C.-N. Chen, W.-H. Lin, Y.-H. Chen, T.-H. Chung, and M.-C. Wu, J. Vacuum Sci. Tech. B **26**, 1831 (2008).

83. C.-C. Tseng, S.-T. Chou, Y.-H. Chen, C.-N. Chen, W.-H. Lin, T.-H. Chung, S.-Y. Lin, P.-C. Chiu, J.-I. Chyi and M.-C. Wu, IEEE Photon. Technol. Lett. **20**, 1240 (2008).

84. A. D. Wieck and K. Ploog, Appl. Phys. Lett. **56**, 928 (1990).

85. J. Nieder, A. D. Wieck, P. Grambow, H. Lage, D. Heitmann, K. V. Klitzing, and K. Ploog, Appl. Phys. Lett. **57**, 2695 (1990).

86. H. W. Schumacher, U. F. Keyser, U. Zeither, R. J. Haug, and K. Eberl,, Appl. Phys. Lett. **75**, 1107 (1999).

87. T.-H. Chung, W.-H. Liao, and S.-Y. Lin, J. Appl. Phys. **108**, 094316 (2010).

88. T.-H. Chung, S.-H. Chen, W.-H. Liao, and S.-Y. Lin, IEEE Electron Device Lett. **31**, 1227 (2010).

89. T.-H. Chung, W.-H. Lin, Y.-K. Chao, and S.-Y. Lin, IEEE Electron Device Lett. **33**, 1129 (2012).

90. S. M. Sze and K. K. Ng, *Physics of Semiconductor Devices*, 3rd ed. pp. 36-38 (New York, NY, USA: Wiley,2007).

91. Y.-A. Liao, W.-H. Lin, Y.-K. Chao, W.-H. Chang, J.-I. Chyi, and S.-Y. Lin, IEEE Electron Device Lett. **34**, 780 (2013).

92. L. Guo, E. Leobandung, S. Y. Chou, Science **275**, 649 (1997).

LIST OF PUBLICATIONS

A. Referred Papers

1. W.-H. Chang, **Y.-A. Liao**, W.-T. Hsu, M.-C. Lee, P.-C. Chiu, and J.-I. Chyi, "*Carrier dynamics of type-II InAs/GaAs quantum dots covered by a thin $GaAs_{1-x}Sb_x$ layer*", Appl. Phys. Lett. **93**, 033107 (2008)

2. **Y.-A. Liao**, W.-T. Hsu, P.-C. Chiu, J.-I. Chyi, and W.-H. Chang, "*Effects of thermal annealing on the emission properties of type-II InAs/GaAsSb quantum dots*", Appl. Phys. Lett. **94**, 053101 (2009)

3. **Y.-A. Liao**, W.-T. Hsu, M.-C. Lee, P.-C. Chiu, J.-I. Chyi, and W.-H. Chang, "*Time-resolved photoluminescence of type-II InAs/GaAs quantum dots covered by a thin $GaAs_{1-x}Sb_x$ layer*", Phys. Stat. Sol. (c), **6**, 1449 (2009)

4. W.-T. Hsu, **Y.-A. Liao**, S.-K. Lu, S.-J. Cheng, P.-C. Chiu, J.-I. Chyi, and W.-H. Chang, "*Tailoring of the wave function overlaps and the carrier lifetimes in InAs/$GaAs_{1-x}Sb_x$ type-II quantum dots*", Physica E **42**, 2524 (2010)

5. W.-S. Liu, H.-M. Wu, **Y.-A. Liao**, J.-I. Chyi, W.-Y. Chen, and T.-M. Hsu, "*High optical property vertically aligned InAs quantum dot structures with GaAsSb overgrown layers*", J. Cryst. Growth **323**, 164 (2010)

6. W.-T. Hsu, **Y.-A. Liao**, F.-C. Hsu, P.-C. Chiu, J.-I. Chyi, and W.-H. Chang "*Effects of GaAsSb capping layer thickness on the optical properties of InAs quantum dots*", Appl. Phys. Lett. **99**, 073108 (2011)

7. **Y.-A. Liao**, W.-T. Hsu, S.-H. Huang, P.-C. Chiu, J.-I. Chyi, and W.-H. Chang, "*Band alignment tuning of InAs quantum dots with a thin AlGaAsSb capping layer*", Appl. Phys. Lett. **102**, 173104 (2013)

8. **Y.-A. Liao**, W.-H. Lin, Y.-K. Chao, W.-H. Chang, J.-I. Chyi, and S.-Y. Lin, "*In-plane gate transistors for photodetector applications*", IEEE Electron Device Lett. **34**, 780 (2013)

9. W.-H. Lin, K.-W. Wang, **Y.-A. Liao**, C.-W. Pao, and S.-Y. Lin, "*The formation mechanisms and optical characteristics of GaSb quantum rings*", J. Appl. Phys. **114**, 053509 (2013)

10. **Y.-A. Liao**, Y.-K. Chao, S.-W. Chang, W.-H. Chang, J.-I. Chyi, and S.-Y. Lin, "*Memory device application of wide-channel in-plane gate transistors with type-II GaAsSb-capped InAs quantum dots*", Appl. Phys. Lett. **103**, 143502 (2013)

B. International Conference Reports

1. **Y.-A. Liao**, W.-T. Hsu, M.-C. Lee, P.-C. Chiu, J.-I. Chyi, and W.-H. Chang, "*Time-resolved photoluminescence of type-II InAs/GaAs quantum dots covered by a thin $GaAs_{1-x}Sb_x$ layer*", The 35th International Symposium on Compound Semiconductors (ISCS2008), Freiburg, Germany

2. **Y.-A. Liao**, W.-T. Hsu, W.-H Chang, P.-C. Chiu, and J.-I. Chyi, "*Spatially indirect excitons in type-II InAs/GaAsSb quantum dots*", The 38th International Symposium on Compound Semiconductors (ISCS2011), Berlin, Germany